



Analysis of aerodynamics under high sideslip angles on the ground

M.G. Cojocaru (INCAS)

Short abstract: Future Sky Safety is a Joint Research Programme (JRP) on Safety, initiated by EREA, the association of European Research Establishments in Aeronautics. The Programme contains two streams of activities: 1) coordination of the safety research programmes of the EREA institutes and 2) collaborative research projects on European safety priorities.

This deliverable is produced by the Project P3 Solutions for Runway Excursions. The main objective is to analyze aircraft aerodynamic characteristics under high sideslip angles (crosswind) during the takeoff/landing ground roll, and to evaluate the longitudinal and lateral aerodynamic coefficients at high sideslip angles due to the lateral gust when the flow separation is fully present. Computational Fluid Dynamics (CFD) evaluations are conducted on two representative aircraft models.

Programme Manager	M.A. Piers, NLR
Operations Manager	L.J.P. Speijker, NLR
Project Manager (P3)	G.W.H. Van Es, NLR

Grant Agreement No.	640597
Document Identification	D3.6
Status	Approved
Version	2.0
Classification	Public

Project: Solutions for runway excursions
Reference ID: FSS_P3_INCAS_D3.6
Classification: Public



This page is intentionally left blank

Contributing partners

Company	Name
INCAS	Stefan Bogos
INCAS	Marius-Gabriel Cojocaru
INCAS	Maria-Cristina Fadgyas
INCAS	Mihai-Victor Pricop
INCAS	Mihaita-Gilbert Stoican

Document Change Log

Version	Issue Date	Remarks
1.0	02-02-2017	First formal release
1.1	13-04-2017	Update by Operations Manager (NLR) to improve the readability (in particular study background/needs, executive summary, introduction and conclusions)
2.0	14-04-2017	Second formal release

Approval status

Prepared by: (name)	Company	Role	Date
M. G. Cojocaru	INCAS	Main Author/Task Leader	22-12-2016
Checked by: (name)	Company	Role	Date
S. Bogos	INCAS	Project Manager for INCAS	22-12-2016
M. V. Pricop	INCAS	Flow Physics Manager	22-12-2016
Approved by: (name)	Company	Role	Date
G.W.H. van Es	NLR	Project Manager (P3)	02-02-2017
L.J.P. Speijker	NLR	Operations Manager	14-04-2017

Acronyms

Acronym	Definition
A/C	Aircraft
AoS	Angle of Side-Slip
cFx	Force coefficient on x direction, body axis
cFy	Force coefficient on y direction, body axis
cFz	Force coefficient on z direction, body axis
cMx	Moment coefficient on x direction, body axis
cMy	Moment coefficient on y direction, body axis
cMz	Moment coefficient on z direction, body axis
CFD	Computational Fluid Dynamics
CG	Centre of Gravity
FME	Fuselage Mounted Engine
MAC	Mean Aerodynamic Chord
RANS	Reynolds Averaged Navier Stokes
WME	Wing Mounted Engine

EXECUTIVE SUMMARY

Problem Area

A runway excursion is the event in which an aircraft veers off or overruns the runway surface during either takeoff or landing. Safety statistics show that runway excursions are the most common type of accident reported annually, in the European region and worldwide. Runway excursions can result in loss of life and/or damage to aircraft, buildings or other items struck by the aircraft. Excursions are estimated to cost the global industry about \$900M every year. There have also been a number of fatal runway excursion accidents. These facts bring attention to the need to identify measures to prevent runway excursions. The European Action Plan for the Prevention of Runway Excursions, which was published in January 2013, provides practical recommendations with guidance materials to reduce the number of runway excursions in Europe. The Action Plan also identified areas where research is needed to further reduce runway excursion risk. One of these areas of research for which additional research is needed is research on the flight mechanics of runway ground operations on slippery runways under crosswind conditions. This is important as accident/incident data on runway excursions shows that the combination of a slippery runway and crosswind significantly increases the likelihood of a veer-off. Pilot guidance material provided by aircraft manufacturers for these operations is often based on simplified simulation models. There is a need to explore the areas of improvement for these simulation models.

Description of Work

The main objectives are to analyse aircraft aerodynamic characteristics under high sideslip angles (crosswind) during take-off/landing ground roll, and to evaluate longitudinal and lateral aerodynamic coefficients at high sideslip angles due to the lateral gust when the flow separation is fully present. Computational Fluid Dynamics (CFD) evaluations are conducted on two representative aircraft models (a fuselage mounted engine configuration and a wing mounted engine configuration). Ground effects are taken into account in the evaluation of the aerodynamic forces due to the lateral gust.

A simulation of the aircraft dynamic control in lateral gust conditions on slippery runways with confident input data and a reliable dynamic model is performed. A specific Computational Fluid Dynamics (CFD) code is used to simulate the flow at a sideslip crosswind angle up to 45 degrees.

Research about the sensitivity of the non-dimensional lateral aerodynamic coefficients at the lateral aircraft geometry is conducted. The CFD study is performed for two different aircraft configurations at several sideslip angles of attack up to 45 degrees, and aerodynamic coefficients in body axes are evaluated and discussed considering the two selected aircraft configurations.

Results & Conclusions

This report is a complex research activity which aims with practical results about the aerodynamic coefficients for two aircraft models in crosswind and ground effects. The aerodynamic forces and moment coefficients were given in an aircraft body system that is clearly presented in the report. The specific notation of the coefficients is also presented in the study. The lateral stability of the Fuselage Mounted Engine (FME) is considered to be normal for the whole span of Angle of Side-Slip (AoS) studied, proved by the value and the behavior of the lateral aerodynamic coefficients. The lateral stability of the Wing Mounted Engine (WME) is considered to be normal for a limited range of AoS (up to 10 degrees). This is due to the small vertical tail volume and engine arrangement in front of the Centre of Gravity.

Applicability

The results of the aerodynamic Computational Fluid Dynamics (CFD) analysis will be used, as input data, in follow-up activities in Future Sky Safety P3, in the WP3.1.4 "Dynamic interaction between aircraft/pilot and ground reactions". Also, the identified shortcomings can be used in future studies to prevent and reduce the risk of accidents caused by the slippery runways under crosswind.

This page is intentionally left blank

TABLE OF CONTENTS

Contributing partners	2
Document Change Log	2
Approval status	2
Acronyms	3
Executive Summary	4
Problem Area	4
Description of Work	4
Results & Conclusions	5
Applicability	5
List of Figures	9
List of Tables	11
1 Introduction	12
1.1. The Programme	12
1.2. Project context	12
1.3. Research objectives	13
1.4. Approach	14
1.5. Structure of the document	15
2 CFD Approach	16
2.1. Governing Equations	16
2.2. Turbulence Modelling	18
2.3. Geometrical Models Description	19
2.3.1. Fuselage Mounted Engines Configuration	20
2.3.2. Wing Mounted Engines Configuration	24
2.4. Meshing	26
2.5. Case Setup	31
3 CFD results	36
3.1. Selection of Mesh Sizing	36
3.2. Results for Fuselage Mounted Engines Configuration	40
3.3. Results for Wing Mounted Engines Configuration	42
3.4. Similarities and Discrepancies in between the Models	44

4	Conclusions and recommendations	46
4.1.	Conclusions	46
4.2.	Recommendations	46
5	References	47

LIST OF FIGURES

FIGURE 1 - ACCIDENT DYNAMICS NUMBER IN 1959-2012, [12]	13
FIGURE 2 - STATISTICS OF THE ACCIDENTS ON THE FLIGHT PHASES: 2003-2012,[12]	13
FIGURE 3 - FLUID ELEMENT FOR CONSERVATION LAWS. [9]	16
FIGURE 4 - MASS FLOW IN AND OUT OF THE FLUID ELEMENT. [9]	17
FIGURE 5 - 3- VIEW DRAWING OF THE FME FROM AAA 3.0	20
FIGURE 6 - WING VIEW FOR FME	20
FIGURE 7 - HORIZONTAL TAIL VIEW FOR FME	21
FIGURE 8 - VERTICAL TAIL VIEW FOR FME	22
FIGURE 9 - FRONT VIEW OF FME CONFIGURATION	23
FIGURE 10 - SIDE VIEW OF FME CONFIGURATION	23
FIGURE 11 - TOP VIEW OF FME CONFIGURATION	24
FIGURE 12 - FRONT VIEW OF WME CONFIGURATION	25
FIGURE 13 - SIDE VIEW OF WME CONFIGURATION	25
FIGURE 14 - TOP VIEW OF WME CONFIGURATION	26
FIGURE 15 - BOUNDARY LAYER SUBDIVISIONS. [15]	28
FIGURE 16 - DOMAIN USED FOR BOTH FME AND WME	29
FIGURE 17 - Y+ ON THE FME UPPER SIDE	29
FIGURE 18 - Y+ ON THE FME LOWER SIDE	30
FIGURE 19 - Y+ ON THE WME UPPER SIDE	30
FIGURE 20 - Y+ ON THE WME LOWER SIDE	31
FIGURE 21 - SIMULATION FLOW CHART	34
FIGURE 22 - REFERENCE VALUES FOR FME CONFIGURATION	34
FIGURE 23 - REFERENCE VALUES FOR WME CONFIGURATION	35
FIGURE 24 - GRID CONVERGENCE OF Mx COEFFICIENT	37
FIGURE 25 - GRID CONVERGENCE OF Fx COEFFICIENT	37
FIGURE 26 - WING MOUNTED ENGINES CONFIGURATION; COARSE GRID	38
FIGURE 27 - WING MOUNTED ENGINES CONFIGURATION; MEDIUM GRID	38
FIGURE 28 - WING MOUNTED ENGINES CONFIGURATION; FINE GRID	39
FIGURE 29 - FUSELAGE MOUNTED ENGINES CONFIGURATION; FINE GRID	39
FIGURE 30 - X-DIRECTION FORCE AND MOMENT COEFFICIENTS	40
FIGURE 31 - Y-DIRECTION FORCE AND MOMENT COEFFICIENTS	40
FIGURE 32 - Z-DIRECTION FORCE AND MOMENT COEFFICIENTS	41
FIGURE 33 - X-DIRECTION FORCE AND MOMENT COEFFICIENTS	42
FIGURE 34 - Y-DIRECTION FORCE AND MOMENT COEFFICIENTS	42
FIGURE 35 - Z-DIRECTION FORCE AND MOMENT COEFFICIENTS	43

FIGURE 36 - CP AT AOS = 0 DEG.	48
FIGURE 37 - CP AT AOS = 20 DEG.	49
FIGURE 38 - CP AT AOS = 30 DEG.	49
FIGURE 39 - CP AT AOS = 40 DEG.	50
FIGURE 40 - CP AT AOS = 0 DEG.	51
FIGURE 41 - CP AT AOS = 10 DEG.	51
FIGURE 42 - CP AT AOS = 15 DEG.	52
FIGURE 43 - CP AT AOS = 20 DEG.	52

LIST OF TABLES

TABLE 1 - FME AND WME CG LOCATIONS	36
TABLE 2 - FME AERODYNAMIC COEFFICIENTS	41
TABLE 3 - WME AERODYNAMIC COEFFICIENTS	43
TABLE 4 - FME CMZ BREAKDOWN AT AOS 20, 30 AND 35 DEG	44
TABLE 5 - WME CMZ BREAKDOWN AT AOS 5, 15 AND 25 DEG	45

1 INTRODUCTION

1.1. The Programme

FUTURE SKY SAFETY is a Joint Research Programme (JRP), initiated by EREA, the association of European Research Establishments in Aeronautics. The Programme contains two streams of activities: coordination of the safety research programmes of EREA institutes and collaborative research projects on European safety priorities. The Programme research focuses on four main topics:

- Building ultra-resilient vehicles and improving the cabin safety
- Reducing risk of accidents
- Improving processes and technologies to achieve near-total control over the safety risks
- Improving safety performance under unexpected circumstance

The Programme will also help coordinate the research and innovation agendas of several countries and institutions, as well as create synergies with other EU initiatives in the field (e.g. SESAR, Clean Sky 2).

1.2. Project context

This study is included in the project Solutions for runway excursions (P3) and is related to a problem that is linked with the topic of the runway excursions: aerodynamic forces evaluation at high sideslip angles on the ground roll at Take off and Landing.

A runway excursion is the event in which an aircraft veers off or overruns the runway surface during either take-off or landing. Safety statistics show that runway excursions are the most common type of accident reported annually, in the European region and worldwide. There are at least two runway excursions each week worldwide. Runway excursions are a persistent problem and their numbers have not decreased in more than 20 years. Runway excursions can result in loss of life and/or damage to aircraft, buildings or other items struck by the aircraft. Excursions are estimated to cost the global industry about \$900M every year. There have also been a number of fatal runway excursion accidents. These facts bring attention to the need to identify measures to prevent runway excursions.

“Flightpath 2050 Europe’s Vision for Aviation” shows that up to 2050, the European air transport system must prove less than one accident per ten million commercial aircraft flight. The Figure 1, that was extracted from a Boeing Report, ref.[12], present information about the dynamics of the accident numbers over the last 50 years. Between 2010 and 2012 there were reported, annually, 5 accidents per ten million of flights. Statistical studies on the number of flight accidents in the period 2003-2012 shows that 16% of accidents occur during takeoff and initial climb and 41% during the final approach and landing. Figure 2, from ref [12], provides details that exemplify the distribution of accidents phases of flight.

Accident Rates and Onboard Fatalities by Year Worldwide Commercial Jet Fleet – 1959 Through 2012

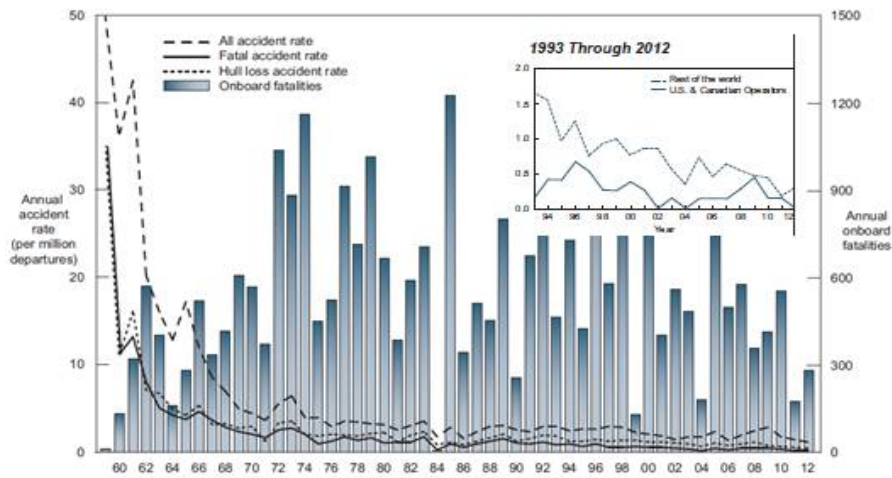


Figure 1 - Accident Dynamics number in 1959-2012, [12]

Fatal Accidents and Onboard Fatalities by Phase of Flight Worldwide Commercial Jet Fleet – 2003 Through 2012

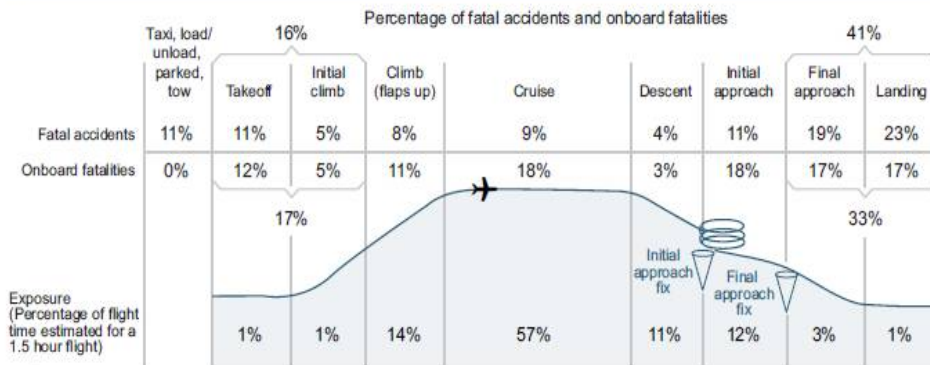


Figure 2 - Statistics of the accidents on the Flight Phases: 2003-2012,[12]

1.3. Research objectives

The Research Objectives from this report are included in the first research topic from the European Action Plan for the Prevention of Runway Excursions, i.e. research on the flight mechanics of runway ground operations on slippery runways under crosswind conditions.

The main objectives are to analyse aircraft aerodynamic characteristics under high sideslip angles (crosswind) during take-off/landing ground roll, and to evaluate longitudinal and lateral aerodynamic coefficients at high sideslip angles due to the lateral gust when the flow separation is fully present. Computational Fluid Dynamics (CFD) evaluations are conducted on two representative aircraft models (a fuselage mounted engine configuration and a wing mounted engine configuration). Ground effects will be taken into account in the evaluation of the aerodynamic forces due to the lateral gust.

1.4. Approach

Most of the publicly known research and development on the flight mechanics of runway ground operations on slippery runways under crosswind conditions was done by NASA and NATO. These study results will be examined to identify possible shortcomings, and as input for the further analysis and aircraft ground model improvements. Past research and development efforts using instrumented test aircraft have concentrated on defining the braking problem while, because of safety constraints, the ground directional control aspect has proven to be more difficult to study using test aircraft.

Instead widespread use is made of ground-based simulation to model aircraft ground directional control behaviour under crosswind conditions. Previous research has shown that the basis of a successful simulation of the ground-roll lies in the mathematical model which accurately represents the component elements and the inter-action between them. The behaviour of the aircraft on the ground is greatly influenced by the forces generated between the tyres and the runway, and the transmission of these forces through the landing gear to the airframe.

To increase the level of the confidence for the dynamic simulation of the aircraft rolling on the runway, when the lateral gust sideslip are presented, a detailed CFD simulation will be developed assuming specific "robust models" for a real simulation.

The objective of this work is to improve the quality of the aerodynamic data definition for an airplane in the "Flaps down" configuration". The following hypotheses are taken into account:

- A fine "aerodynamic mesh" was developed, according with two real aircraft configuration;
- The nonlinear flow separation effects at high sideslip angles were simulated
- *Ground effect* on the aircraft aerodynamics will be introduced by the CFD specific boundary conditions for the surface that simulates the runway;

The aircraft models that will be considered in CFD aerodynamic simulation are closed with the most typical airplane families' configuration:

- Aircraft with two engines on the fuselage, with T tail configuration;
- Aircraft with two engines on the wing.

So, the results of this study permit a good visibility about the "formal" aerodynamic behavior of the flow at high sideslip angles, with ground effect for two typical A/C families: with two engines placed on the fuselage or two engines placed on the wings.

In the most common situation, the aerodynamic simulation at the flow around an aircraft configuration, at small sideslip angles were made more in wind tunnel facilities, in Cruise or Flaps down configurations, without ground effect.

However, ref [13] presents some experimental results at high sideslip angles, 30-40 deg., for some commercial aircraft: MD 80, Boeing 737-400 and DHC-8. The theoretical CFD evaluation of the lateral sideslip flow is based on the "high-alpha flow analogy" specific to the combat aircraft. The lateral flow around the fuselage and the dorsal fin system is treated, similar with the symmetric flow at high incidence angle. This assumption has only a qualitative value due to the hypothesis and models that were taken into account.

In ref [14], the ground effects that were used in the dynamic simulation for a Jet Transport aircraft, in crosswind flow, are based only on the experimental data.

It seems that is a lack for wind tunnel tests or full CFD simulations of the flow at high sideslip angles, with ground effect for an aircraft configuration with flaps extended. So, this study intends to complete the missing information about the aerodynamic in the presence of the lateral gust for an aircraft at Take off and Landing roll.

1.5. Structure of the document

The document is divided in four chapters. The first chapter is dedicated to the revelation of the objectives of the analysis performed within this Task of the project and the approach that will be followed in order to get the lateral and longitudinal aerodynamic coefficients.

The second chapter is dedicated to the CFD approach. The governing equations, together with the turbulence modelling, meshing and case setup are reported in order to have an ensemble view of the numerical analysis performed.

The third chapter is dedicated to the results obtained, to the criteria for selecting mesh sizing, to the evaluation and comparative analysis of all the aerodynamic coefficients for the two different aircraft configurations, fuselage mounted engine and, respectively, wing mounted engine.

The last chapter is dedicated to the conclusions and the recommendations that will be extracted following the numerical analysis performed.

2 CFD APPROACH

2.1. Governing Equations

The fundamental governing equations of fluid dynamics, known as Navier-Stokes equations, include mass, momentum and energy conservation laws. They can be derived from applying these physical principles to a finite control volume of fluid or to a very small fluid element, as seen in Figure 3.

For the governing equations of fluid flow, the conservation laws of physics are applied:

- The mass of a fluid is conserved;
- Newton's second law: the rate of change of momentum equals the sum of the forces on a fluid particle;
- First law of thermodynamics: the rate of change of energy is equal to the sum of the rate of heat addition to and the rate of work done on a fluid particle.

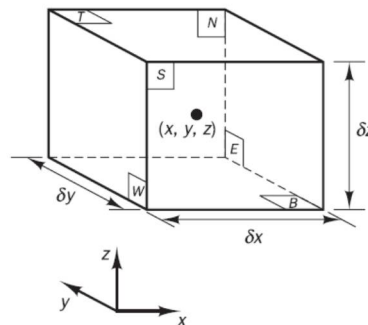


Figure 3 - Fluid element for conservation laws. [9]

1. For the mass conservation equation that rate of increase of mass in fluid equals net rate of flow of mass into element fluid element Figure 4. Doing the above stated results in the **unsteady, three-dimensional mass conservation or continuity equation** at a point in a **compressible fluid**:

$$\frac{\partial \rho}{\partial t} + \frac{\partial(\rho u)}{\partial x} + \frac{\partial(\rho v)}{\partial y} + \frac{\partial(\rho w)}{\partial z} = 0$$

2. Newton's second law states that the rate of change of momentum of a fluid particle equals the sum of the forces on that particle. Setting the rate of change of x -momentum of the fluid particle equal to the total force in the x -direction on the element (due to surface stresses) plus the rate of increase of x -momentum results in x -component of the momentum equation:

$$\rho \frac{Du}{Dt} = -\frac{\partial p}{\partial x} + \frac{\partial}{\partial x} \mu \left[2 \frac{\partial u}{\partial x} - \frac{2}{3} \text{div } \mathbf{V} \right] + \frac{\partial}{\partial y} \mu \left[\frac{\partial u}{\partial y} + \frac{\partial v}{\partial x} \right] + \frac{\partial}{\partial z} \mu \left[\frac{\partial u}{\partial z} + \frac{\partial w}{\partial x} \right] + S_x$$

, and analogously for y and z directions:

$$\rho \frac{Dv}{Dt} = -\frac{\partial p}{\partial y} + \frac{\partial}{\partial y} \mu \left[2 \frac{\partial v}{\partial y} - \frac{2}{3} \text{div } \mathbf{V} \right] + \frac{\partial}{\partial x} \mu \left[\frac{\partial u}{\partial y} + \frac{\partial v}{\partial x} \right] + \frac{\partial}{\partial z} \mu \left[\frac{\partial v}{\partial z} + \frac{\partial w}{\partial y} \right] + S_y$$

$$\rho \frac{Dw}{Dt} = -\frac{\partial p}{\partial z} + \frac{\partial}{\partial z} \mu \left[2 \frac{\partial w}{\partial z} - \frac{2}{3} \text{div } \mathbf{V} \right] + \frac{\partial}{\partial y} \mu \left[\frac{\partial w}{\partial y} + \frac{\partial v}{\partial z} \right] + \frac{\partial}{\partial x} \mu \left[\frac{\partial u}{\partial z} + \frac{\partial w}{\partial x} \right] + S_z$$

, where we have: $\mathbf{V} = u \cdot \vec{i} + v \cdot \vec{j} + w \cdot \vec{k}$ as the velocity vector, and the terms S_x, S_y, S_z are source terms for the momentum equations.

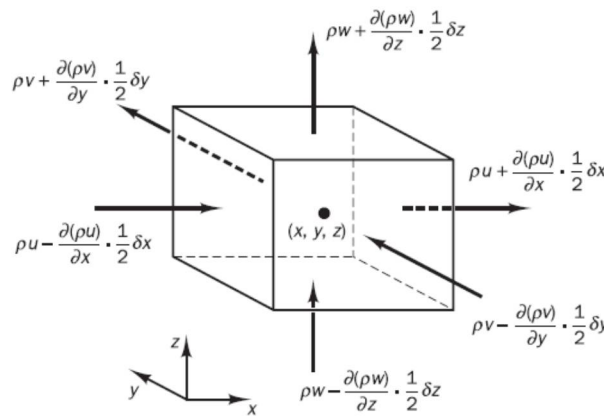


Figure 4 - Mass flow in and out of the fluid element. [9]

- The **first law of thermodynamics** states that the rate of change of energy of a fluid particle is equal to the rate of work done on the particle added together with the rate of heat addition to the fluid particle:

$$\rho \frac{DE}{Dt} = -\text{div}(p\mathbf{V}) + \left[\frac{\partial(u\tau_{xx})}{\partial x} + \frac{\partial(u\tau_{yx})}{\partial y} + \frac{\partial(u\tau_{zx})}{\partial z} + \frac{\partial(v\tau_{xy})}{\partial x} + \frac{\partial(v\tau_{yy})}{\partial y} + \frac{\partial(v\tau_{zy})}{\partial z} + \frac{\partial(w\tau_{xz})}{\partial x} + \frac{\partial(w\tau_{yz})}{\partial y} + \frac{\partial(w\tau_{zz})}{\partial z} \right] + \text{div}(k \text{ grad } T) + S_E$$

, where we have used the following notations:

$$\tau_{xx} = 2\mu \left(\frac{\partial u}{\partial x} - \frac{2}{3} \text{div } \mathbf{V} \right), \tau_{yy} = 2\mu \left(\frac{\partial v}{\partial y} - \frac{2}{3} \text{div } \mathbf{V} \right), \tau_{zz} = 2\mu \left(\frac{\partial w}{\partial z} - \frac{2}{3} \text{div } \mathbf{V} \right)$$

$$\tau_{xy} = \tau_{yx} = \mu \left(\frac{\partial u}{\partial y} + \frac{\partial v}{\partial x} \right), \tau_{xz} = \tau_{zx} = \mu \left(\frac{\partial u}{\partial z} + \frac{\partial w}{\partial x} \right), \tau_{zy} = \tau_{yz} = \mu \left(\frac{\partial v}{\partial z} + \frac{\partial w}{\partial y} \right)$$

2.2. Turbulence Modelling

The levels of approximation when solving the Navier-Stokes equations can be interpreted as the trade-off of CPU time and accuracy, the difficulty of grid generation being taken into consideration as well. One of the most used methods today due to its proven broad range of applicability and robustness it is the RANS approach. The RANS solution procedure is based on the assumption that the flow is turbulent and that the solution variables can be decomposed in an average part and a fluctuation. Examples for the velocity components and other scalar quantities are:

$$u_i = \bar{u}_i + u'_i \text{ and } \phi = \bar{\phi} + \phi'$$

By substituting the flow variables with such equations into the instantaneous continuity and momentum equations and taking a time average gives the so called Reynolds-averaged Navier-Stokes (RANS) equations, which can be written as for example for the momentum equation:

$$\frac{\partial(\rho u_i)}{\partial t} + \frac{\partial(\rho u_i u_j)}{\partial x_j} = -\frac{\partial p}{\partial x_i} + \frac{\partial}{\partial x_j} \left[\mu \left(\frac{\partial u_i}{\partial x_j} + \frac{\partial u_j}{\partial x_i} - \frac{2}{3} \delta_{ij} \frac{\partial u_l}{\partial x_l} \right) \right] + \frac{\partial}{\partial x_j} (-\rho \overline{u'_i u'_j})$$

The velocities and other solution variables now represent the time-averaged values. Additional terms now appear that represent the effects of turbulence, these terms are grouped in the so called turbulent Reynolds stresses. Turbulent Reynolds stresses $\tau_{ij,t}$ need now to be modelled, and in most of the cases this means using the so called Boussinesq hypothesis:

$$\tau_{ij,t} = \frac{2}{3} \mu_t S_{ij} - \frac{2}{3} k \delta_{ij}, \text{ where } S_{ij} \text{ is the mean strain rate tensor and } \mu_t \text{ is the eddy viscosity.}$$

The advantage of this approach is represented by the low computational cost associated with the computation of the turbulent viscosity. RANS method is the most affordable turbulence method regarding CPU requirements, as it does not solve the turbulent motion of small scales directly, but it does have its limitations regarding accuracy and reliability especially when it comes to low Reynolds number flows and unstable flows. Despite the limitations all the findings in this project are based on RANS approach. From the RANS models the **Realizable k- ϵ** turbulence model is selected to be used in this project. This model differs from the standard k- ϵ by:

- Contains an alternative formulation for the turbulent viscosity;
- For the dissipation rate, ϵ , a modified transport equation has been derived for the transport of the mean-square vorticity fluctuation.

The most notable advantages and disadvantages are:

- Performance exceeds the standard k- ϵ model
- Compressibility terms can be included

- Suitable for complex flows with large strain rates (rotation, separation), such as those encountered in this application.
- Suffers limitations of an isotropic eddy-viscosity model.

The modelled transport equations k for ϵ and in the Realizable model are

$$\frac{\partial}{\partial t}(\rho k) + \frac{\partial}{\partial x_j}(\rho k u_j) = \frac{\partial}{\partial x_j} \left[\left(\mu + \frac{\mu_t}{\sigma_k} \right) \frac{\partial k}{\partial x_j} \right] + G_k + G_b - \rho \epsilon - Y_M - S_k$$

$$\frac{\partial}{\partial t}(\rho \epsilon) + \frac{\partial}{\partial x_j}(\rho \epsilon u_j) = \frac{\partial}{\partial x_j} \left[\left(\mu + \frac{\mu_t}{\sigma_\epsilon} \right) \frac{\partial \epsilon}{\partial x_j} \right] + \rho C_{1\epsilon} S \epsilon + \rho C_{2\epsilon} \frac{\epsilon}{k + \sqrt{\epsilon \nu}} - C_{1\epsilon} \frac{\epsilon}{k} C_{3\epsilon} G_b - S_\epsilon$$

, where $C_{1\epsilon} = 1.44$, $C_{2\epsilon} = 1.92$, $C_\mu = 0.09$, $\sigma_k = 1.0$, $\sigma_\epsilon = 1.3$ and $C_1 = \max\left(0.43, \frac{\eta}{\eta+5}\right)$, $\eta = S \frac{k}{\epsilon}$, $S = \sqrt{2S_{ij}S_{ij}}$.

2.3. Geometrical Models Description

The geometries for both FME and WME configurations were adopted from available models from literature [5] or from CFD workshop websites [10, 11]. The FME configuration is intended as a medium-haul fuselage mounted engines aircraft. The WME is an aircraft of similar size to FME with simple trailing edge flaps at 42 deg., but with a few notable differences:

- A more pronounced wing sweep on the WME.
- The distance to the ground from the wing is higher for the WME than for the FME due to the engines.
- The wing dihedral angle on the WME is more pronounced
- The wing flap is composed of two section, inboard and outboard for the WME, Figure 14, whereas for the FME there is a single flap on each wing, Figure 11.
- The fuselage diameter is bigger for the FME (3.3m) than for the WME (3.1m).
- The horizontal tail is mounted at -2 deg. on the FME while on the WME the tail is at 0deg.
- The vertical tail (+ dorsal fin) lateral projection are for the FME is approximately 20% bigger than for the WME.
- The vertical tail volume for WME is less (approximately 0.05) than it should be for such a configuration (approx.. 0.075), with undesired effects on the yaw moment at high AoS.

Regarding the reference system used the current computations and reporting is done in a reference system related to the body axis as shown in Figure 9 to Figure 14.

2.3.1. Fuselage Mounted Engines Configuration

This configuration is based on the literature available models for fuselage mounted engines [5, 6, 7 and 8]. The horizontal tail setup is at -2deg. The aircraft's wing was modified to include a flap at 42 deg. The flap geometry is taken from the MD 30P/30N airfoil and is positioned on the aircraft's wing without any kind of numerical aerodynamic optimization. The nacelles considered are flow-through nacelles. The vertical tail is based on the NACA 0009 airfoil. The wing root airfoil is based on the NACA 63-212, while the wing tip airfoil is NACA 63-210, and a wing twist of -3 deg. and the dihedral angle is 2.5 deg.

The geometry is scaled and computed in the Advanced Aircraft Analysis software, version 3.0 in order to have a realistic aircraft configuration, see Figure 5, Figure 6, Figure 7 and Figure 8. Afterwards the geometry is inputted into Ansys DesignModeler to be cleaned and to be made ready for meshing.

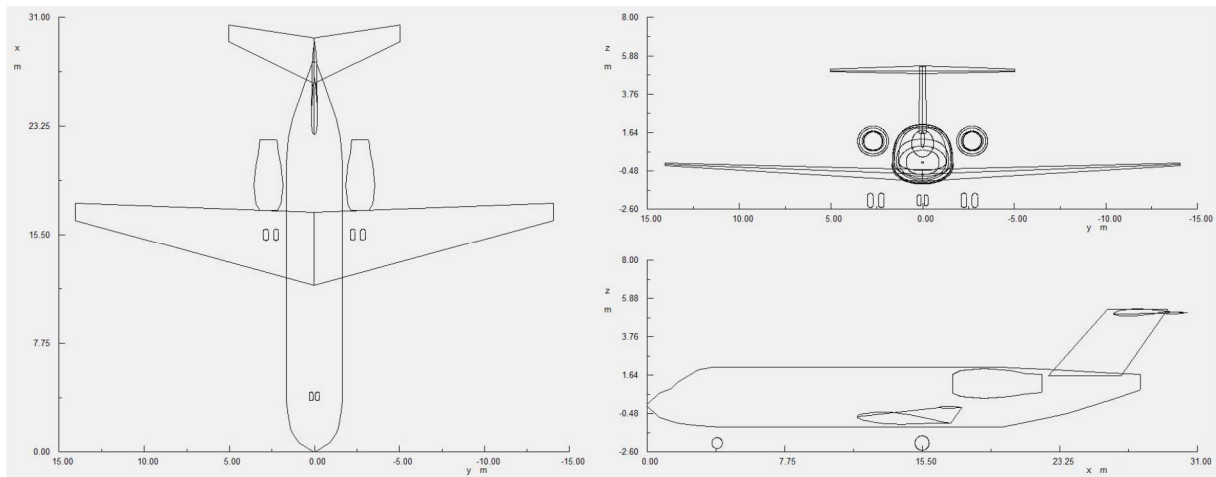


Figure 5 - 3- view drawing of the FME from AAA 3.0

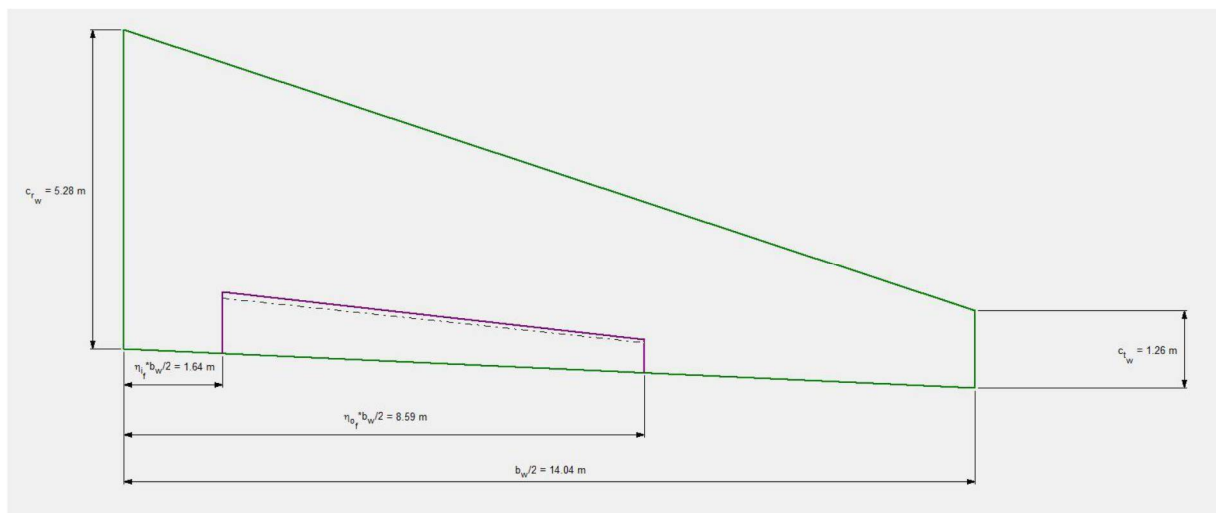


Figure 6 - Wing view for FME

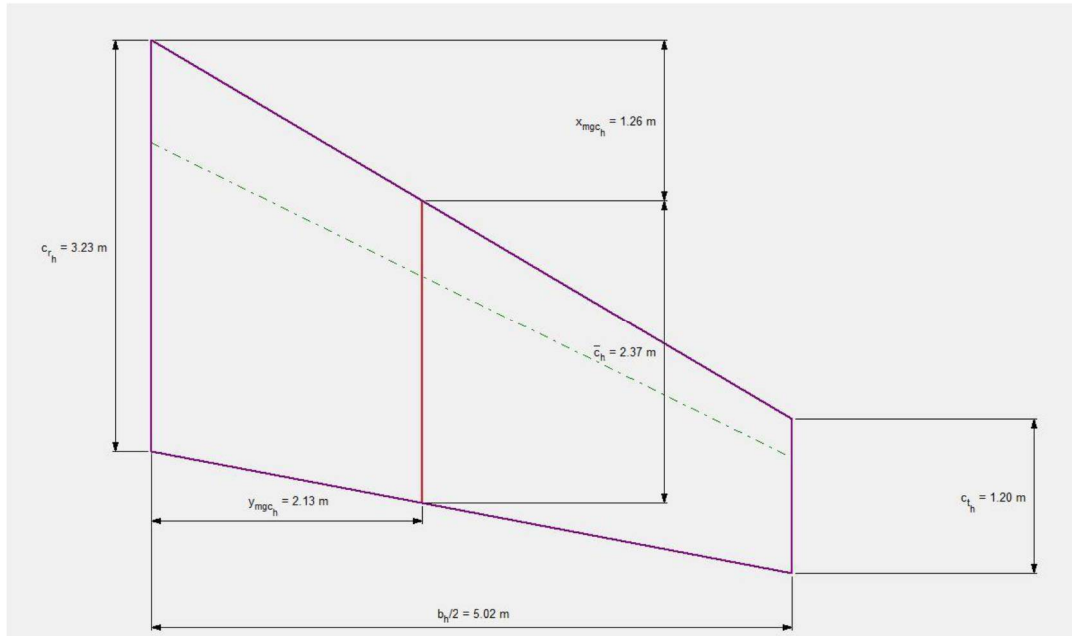


Figure 7 - horizontal tail view for FME

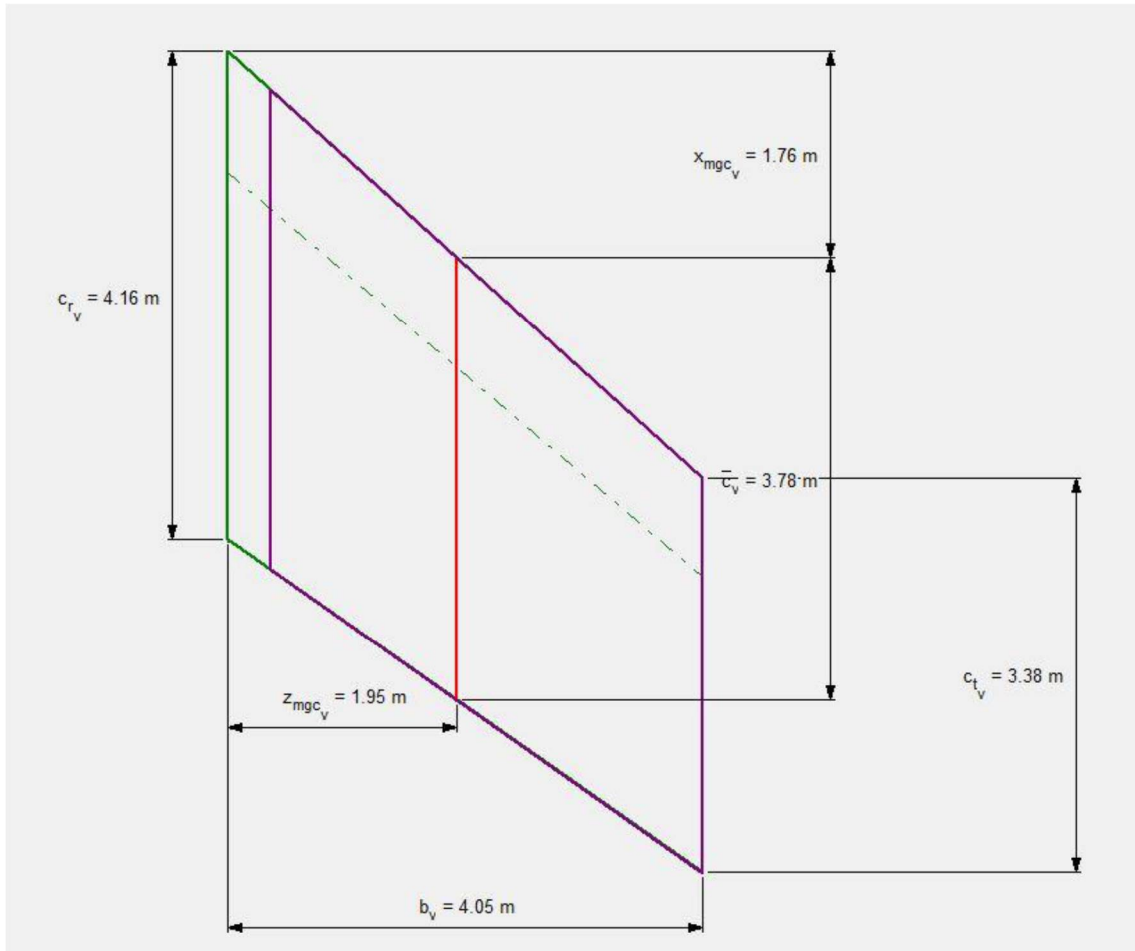


Figure 8 - vertical tail view for FME

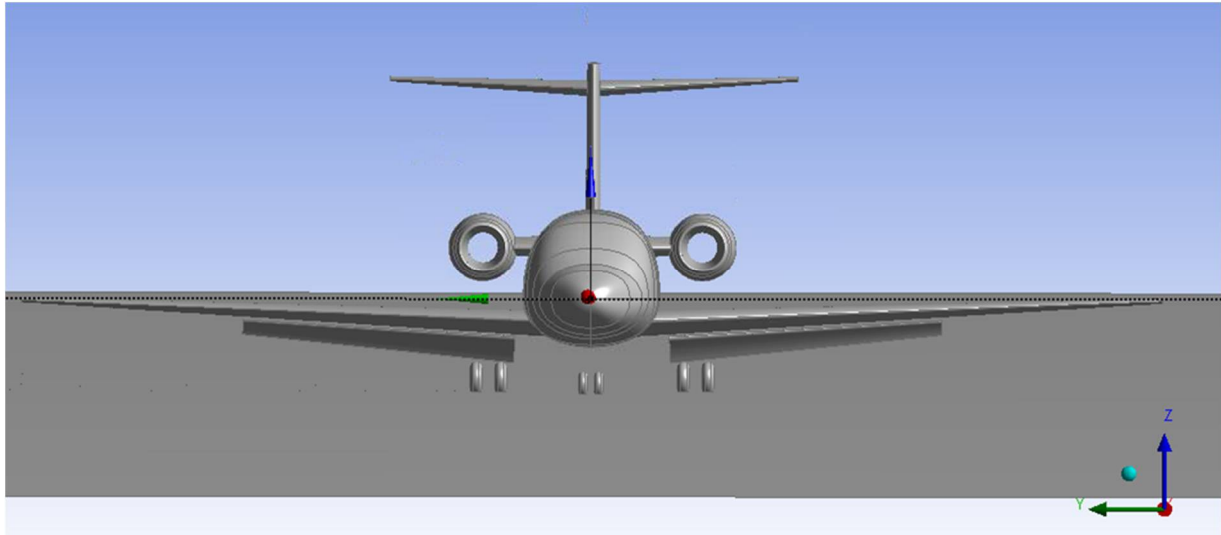


Figure 9 - Front view of FME configuration

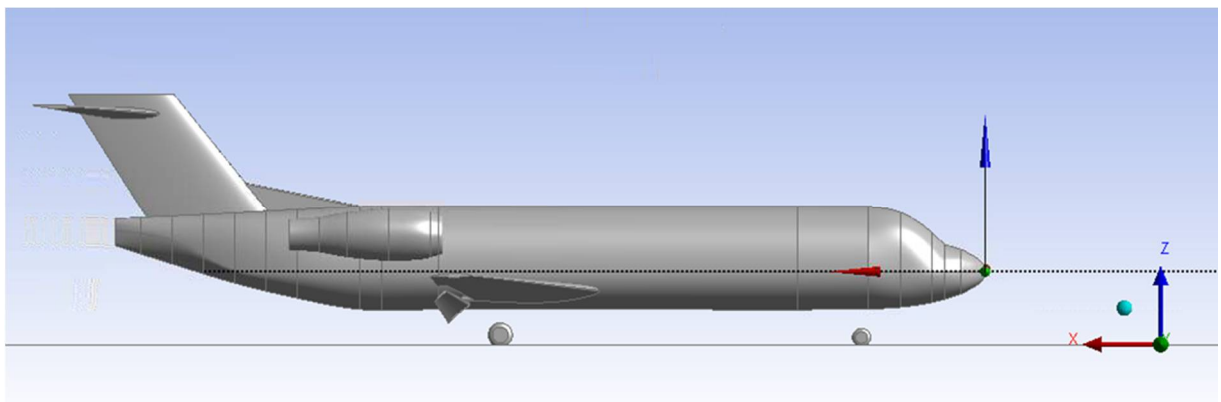


Figure 10 - Side view of FME configuration

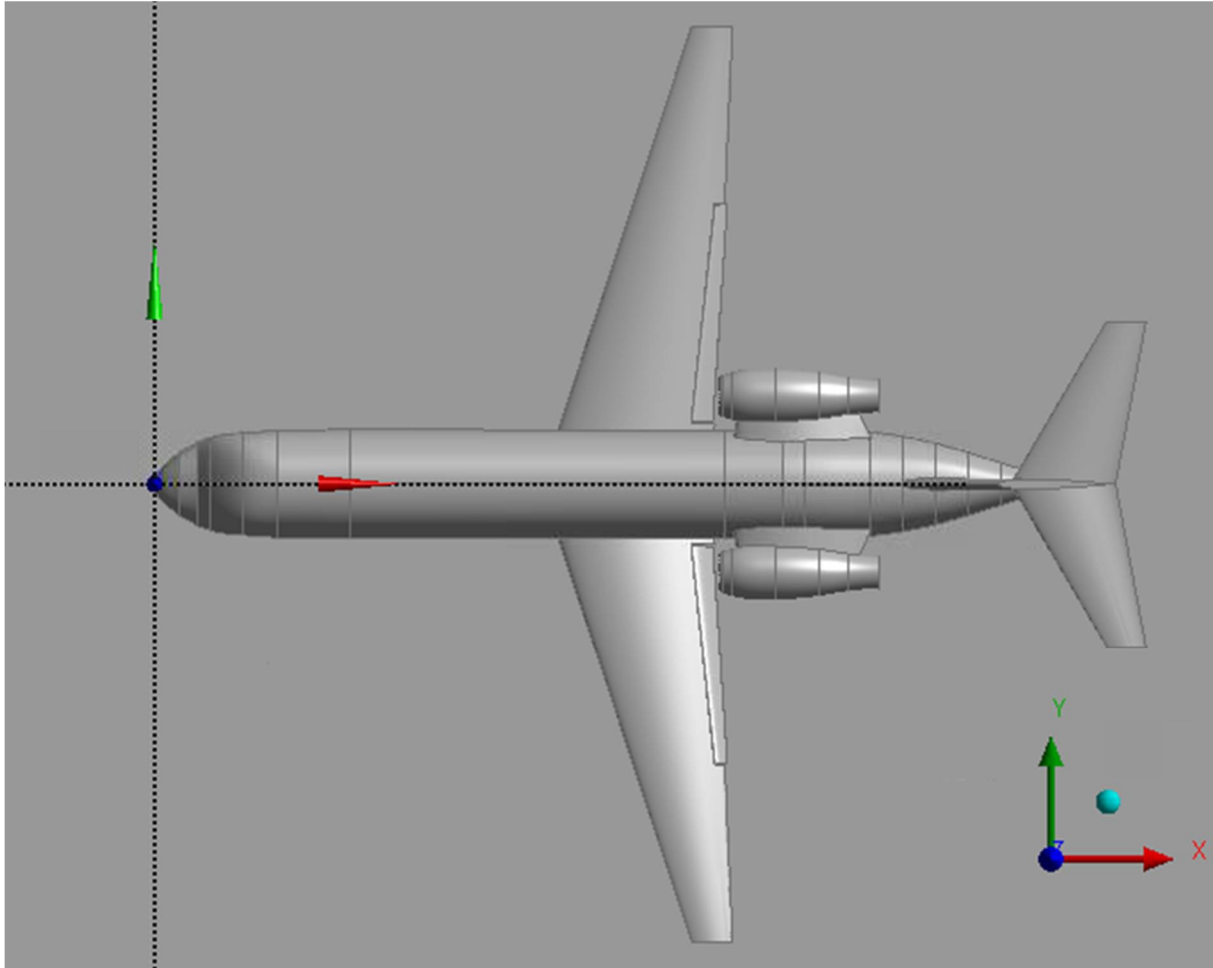


Figure 11 - Top view of FME configuration

2.3.2. Wing Mounted Engines Configuration

This configuration is based on the NASA CRM (Common Research Model) aircraft [10] scaled to 1:2 and with a vertical tail fitted [11]. The horizontal tail setup is at 0deg. The aircraft's wing was modified to include a flap at 42 deg. and split in two sections, outboard and inboard. The flap geometry is taken from the MD 30P/30N airfoil and is positioned on the aircraft's wing without any kind of numerical aerodynamic optimization. The nacelles considered are flow-through nacelles. The reference system is kept the same in x and y direction as available from the reference geometry [10, 11] and only raised in the z direction to create a clearance for the engine nacelles from the ground, and in this way the aircraft nose is situated at $z=3.01$ m in this new reference system where the ground is at $z = 0$ m.

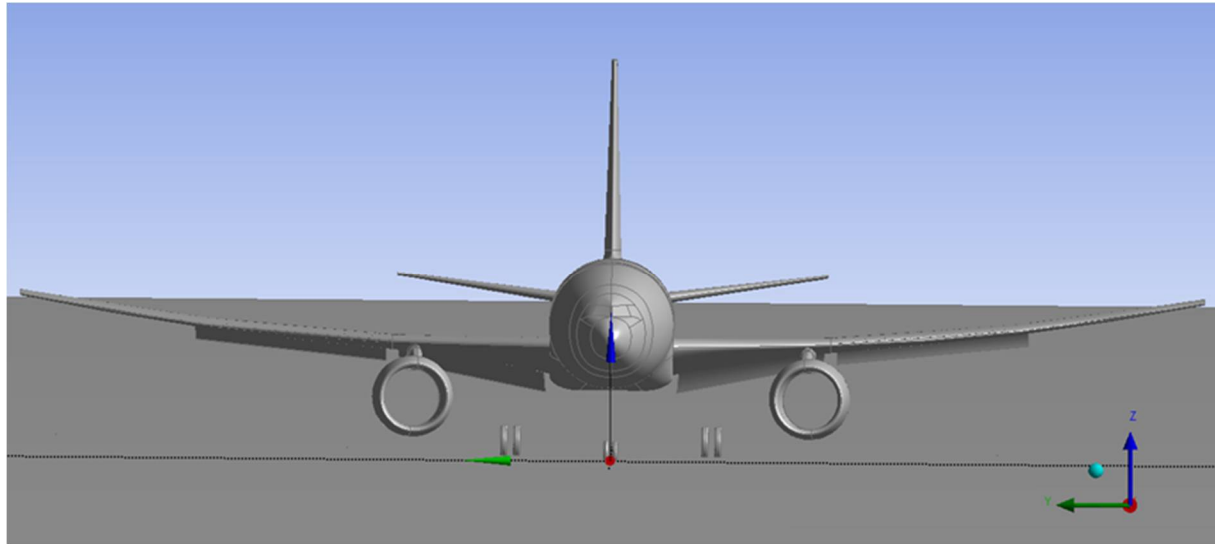


Figure 12 - Front view of WME configuration

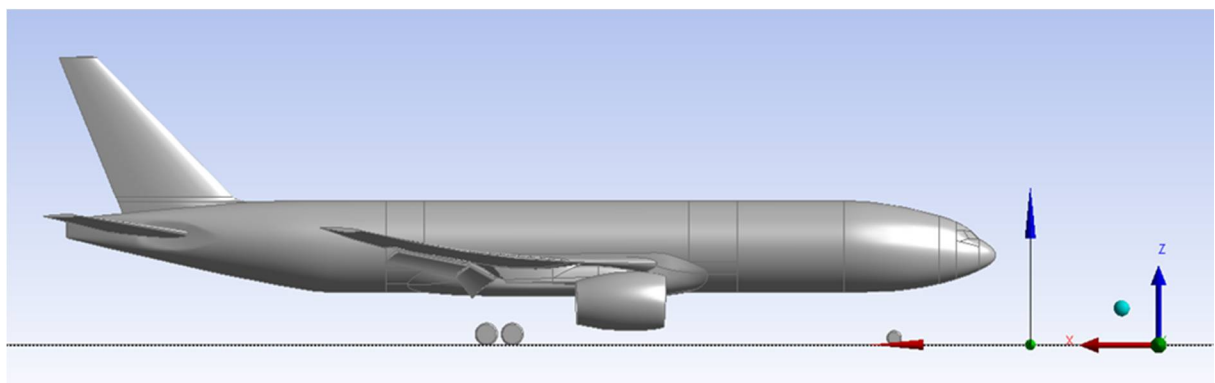


Figure 13 - Side view of WME configuration

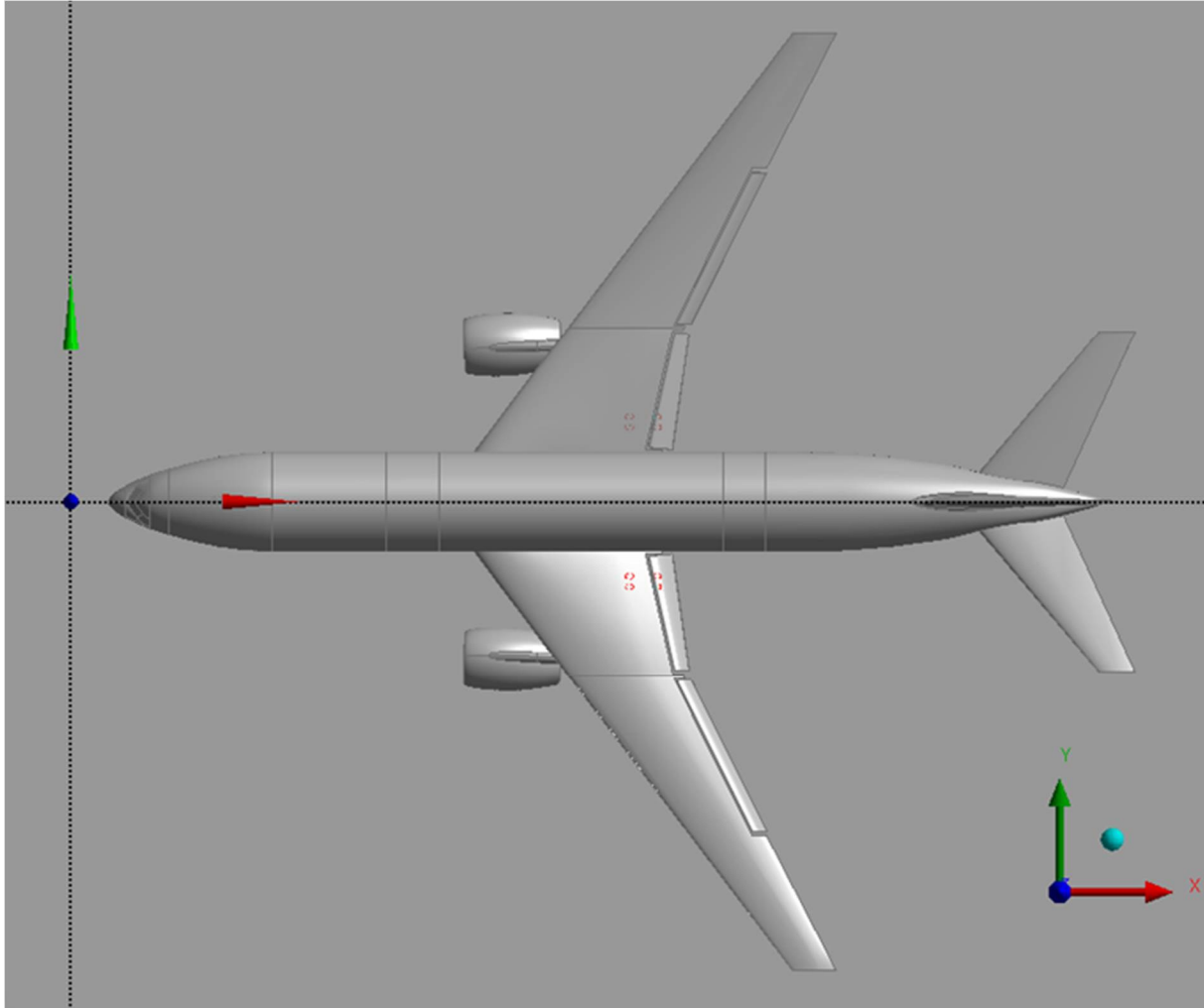


Figure 14 - Top view of WME configuration

2.4. Meshing

For this study unstructured grids were employed in order to perform the aerodynamic analysis, Figure 26, Figure 27 and Figure 28. First a set of three differently refined grids are constructed to verify the grid sensitivity as described in a latter chapter. This check is done to verify if a grid with a lower resolution can be used for crosswind simulations. By doing this, the simulation time can be shortened drastically.

For bot configurations, FME and WME, the same grid considerations hold true. The grids consist of hexahedral elements, generated using Numeca Hexpress. The grid node distribution was carefully

adjusted so as to maintain an acceptable grid skewness and orthogonal quality for all grids. As the main regions of interest, the grids with extra refinement are:

- Leading edges: wing, flap, horizontal tail, vertical tail, dorsal fin
- Trailing edges: wing, flap, horizontal tail, vertical tail, pylons
- Vertical tail upper surface
- Flap surfaces
- Pylon surfaces
- Nacelle surfaces
- Dorsal fin surfaces (only for FME)
- Aircraft fuselage and fairing section
- Nacelle lip, exhaust nozzle

Regarding vorticity and turbulence, the walls represent their main source. Walls produce turbulent momentum and thermal boundary layers (very near-wall regions have the steepest variations). A reliable near-wall modelling is important for most industrial CFD applications, since the usage of very fine mesh (for resolving the steep profiles) is still too expensive for many industrial CFD simulations. The numerical results for turbulent flows are susceptible to the near-wall grid resolution; hence sufficiently fine meshes should be used in these regions. On the other hand, fine meshes in the near-wall region are also a key factor in obtaining the full benefit of the k- ϵ RANS model. Therefore we need to construct a numerical boundary layer near the solid walls. For this by using a y^+ calculator and knowing the desired y^+ (≈ 35) to be in log-law layer, see Figure 15, at the center of the cell, the wall adjacent cell height has been placed within the range of 4×10^{-4} meters for validation cases and for study cases. The growth rate in the numerical boundary layer equals 1.2 for all cases.

In order to validate that the constructed grids fulfill the desired y^+ distribution the Figure 17, Figure 18, Figure 19 and Figure 20 are used, depicting the y^+ distribution for the flow at AoS = 0deg. on both configurations. There we can see that the y^+ value is around the desired one, therefore the use of Non-Equilibrium Wall Functions, described latter on is justified.

A high y^+ model was selected to be used in conjunction with specific wall treatment (functions) in order to reduce the computational time by having a smaller grid size when compared to a low y^+ one.

For fixed-wing aircraft, ground effect has an important contribution for the intended simulation at landing. In theory, the ground effect is the increased lift force and decreased aerodynamic drag that the wing is generating. Flying close to a certain surface at high speed increases the air pressure on the lower surface of the wing, therefore improving the lift-to-drag ratio. This effect is known as the "ram" or "cushion" effect. When an aircraft is flown close to the ground, wingtip vortices are reduced as well due to the obstruction, resulting in a lower induced drag. This improves the lift as well and increases the

speed of the aircraft. In order to take these effects into account, the aircraft is placed on an imaginary runway. The plane is going through the tires in order to assure a good transition for meshing, Figure 10 and Figure 13.

The domain consisting of air is represented by an arbitrary shape; therefore a dome with a radius of 500 meters was created which incorporates the ground and the aircraft geometry. It is important make a trade-off when choosing the size, in order to lower the simulation time but at the same time to include sufficient volume that is relevant for flow simulation and minimize the effect of boundary conditions imperfection onto the solution by placing the far-field boundary condition at roughly 150 MAC in any direction.

The smallest surface element for the Fine grid for both configuration (FME and WME) is approximately 5mm, while for the Medium grid is 7.5mm, and for the Coarse one 11.25 mm.

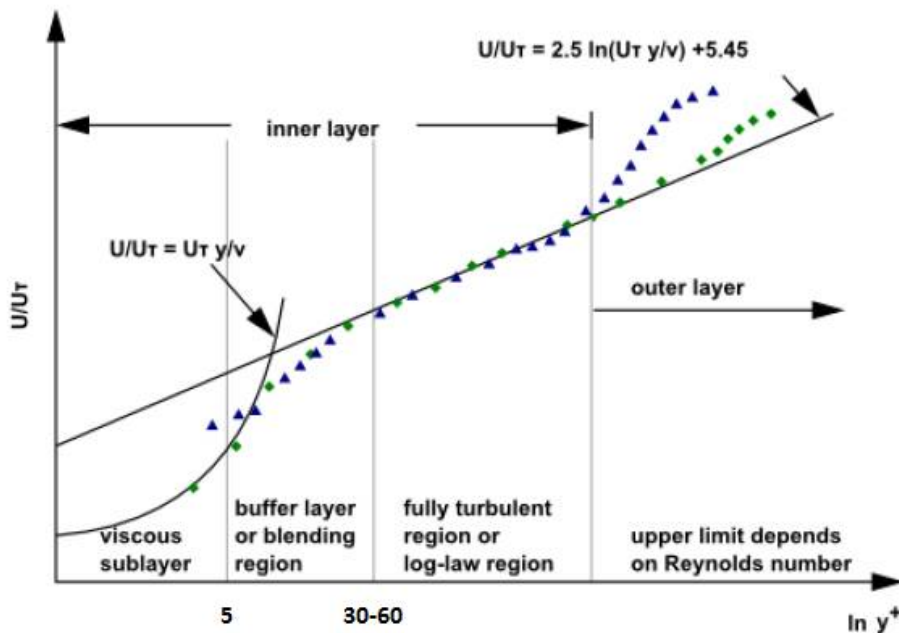


Figure 15 - Boundary layer subdivisions. [15]

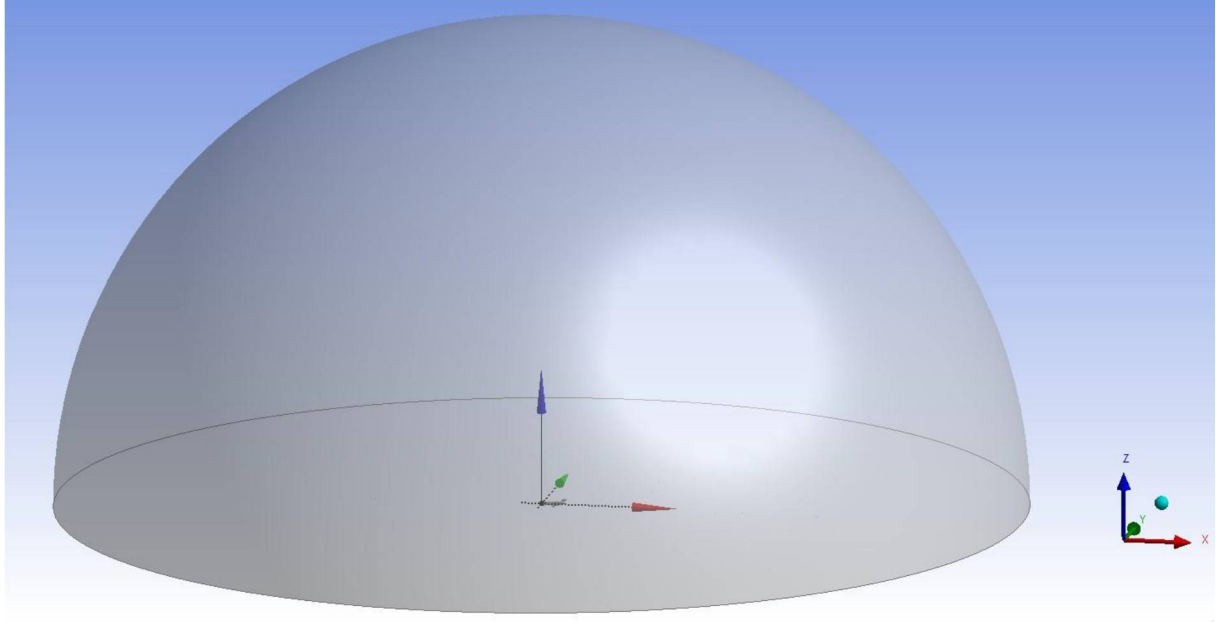


Figure 16 - Domain used for both FME and WME.

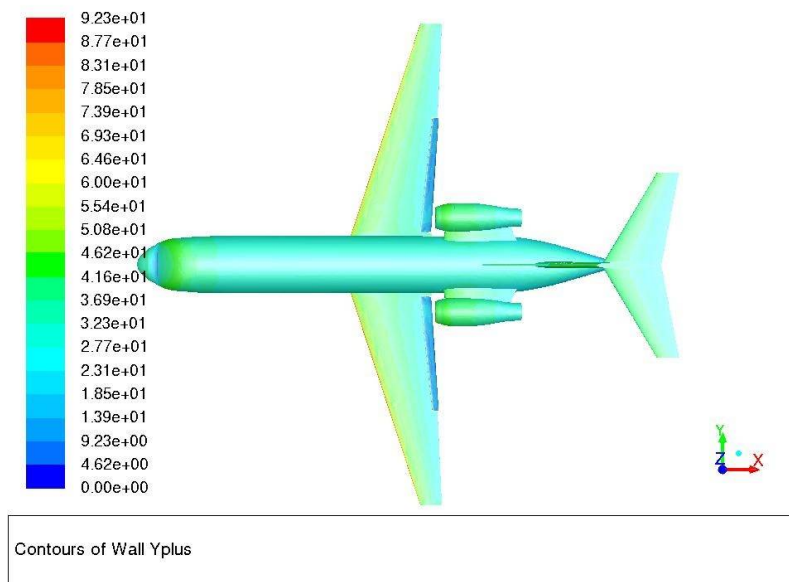
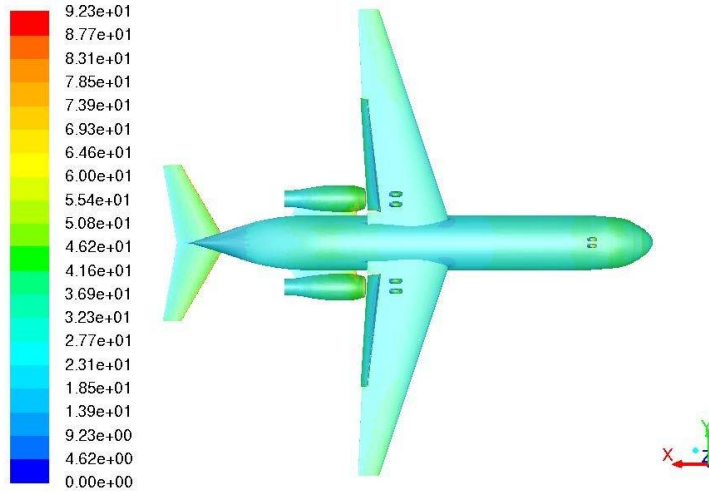
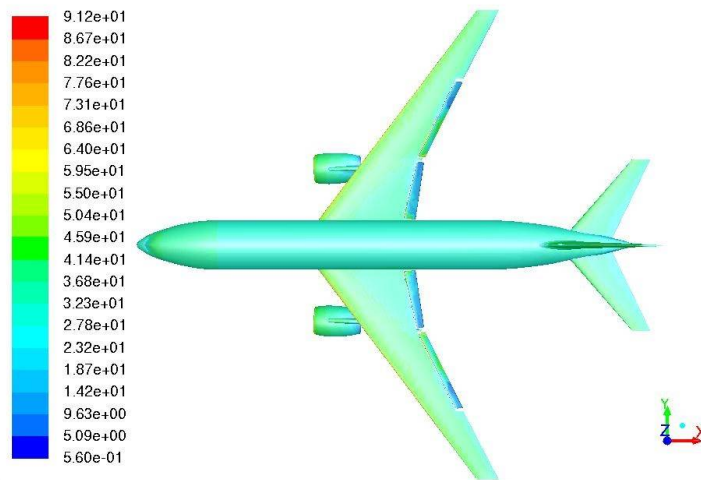


Figure 17 - Y+ on the FME upper side



Contours of Wall Yplus

Figure 18 - Y+ on the FME lower side



Contours of Wall Yplus

Figure 19 - Y+ on the WME upper side

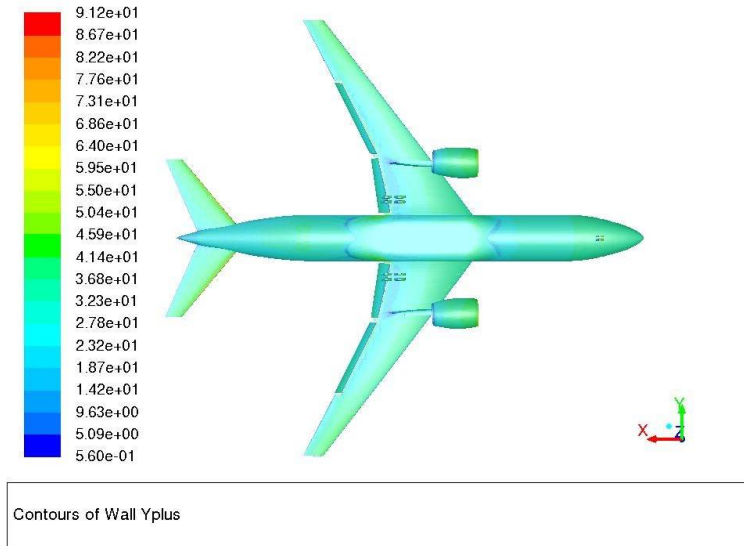


Figure 20 - Y+ on the WME lower side

2.5. Case Setup

All the simulations were carried out on the SGI UV2000 computer cluster at INCAS using 272 CPU cores and the Ansys Fluent V16.2 software. The Ansys Fluent software is a CFD product that uses the finite volume method to solve the Navier-Stokes equations. It uses up to third order accuracy in space and second order in time. The density-based solver is used within the implicit steady time and absolute velocity formulation. This solver it is used for solving the governing equations of momentum, continuity, and energy. If necessary, governing equations for other scalars such turbulence equations are solved afterwards (sequentially). A number of iterations of the solution loop must be done before a converged solution can be obtained, due to the fact that the governing equations are non-linear, as well as coupled.

Simulations were carried out with a free-stream Mach number $M_\infty = 0.21165$. This value is obtained from an assumed touchdown speed of 72 m/s, in order to simulate a landing at high speed and to take into account compressibility. The flow is fully turbulent and the used Reynolds number at which the test is performed is $Re = 16.8 \times 10^6$, based on the free flow condition and the reference chord length (MAC):

$$MAC = 3.5m$$

$$V_\infty = 72 \text{ m/s (approx. 140 knots)}$$

$$\rho = 1.225 \text{ kg/m}^3$$

$$P_{\infty} = 101325 \text{ Pa}$$

$$\mu = 1.8375 \cdot 10^{-5} \text{ kg/ms}$$

The models used for the simulation are:

- Energy equations is solved coupled with the continuity and momentum equations.
- Viscous options:
 - *k-ε realizable* turbulence model
 - non-equilibrium wall functions
 - production limiter option is activated with the production limiter clip factor of 10
 - Energy/wall Prandtl number are set to 0.85

The near wall treatment allows as to use a grid with a y^+ value higher than 30 and is based on the wall function approach, and it is materialized by choosing a non-equilibrium wall function. The key features of the non-equilibrium wall functions are:

- Launder's and Spalding's logarithmic law of the wall is made to account for pressure gradient effects
- The budget of turbulent kinetic energy production and destruction in the wall adjacent cells is based on a two-layer concept that splits their treatment in two regions separated by a y^+ value of 11.225

The main advantage of the non-equilibrium wall function over the standard one is that it is capable to partially account for pressure gradients associated with complex flows involving separation, reattachment and impingement, where the flow and turbulence are subjected to fast changes. In this cases improvements of skin friction (wall-shear) are expected to be obtained over the standard wall function.

The production limiter option is used to improve (limit) the production of turbulent kinetic energy near stagnation (detachment and reattachment) points. Since the flow can have massive separation regions this feature is strongly advised to be activated.

The material used for the simulation is air, with the density varying with pressure according to the ideal-gas law, constant specific heat (C_p), molecular weight and thermal conductivity (k), and Sutherland viscosity. This type of viscosity variation is a relation between the dynamic viscosity μ and the absolute temperature T of an ideal gas. Sutherland's law gives fairly accurate results with a low error for the range of temperature variations encountered in this flow.

The boundary conditions are important in defining the direction and magnitude of the flow. The far field is defined as a pressure-far-field boundary condition, having as characteristics a temperature of

288.15 K, Mach number of 0.21165 and gauge pressure equal to 0 (due to the fact that the operating pressure is already set at 101325 Pa):

$$P_{absolute} = P_{operating} + P_{gauge}$$

In order to define the headwind acting on the aircraft, the components of flow direction are set at: X=1; Y=0; Z=0 for AoS = 0 deg.

For solution methods the implicit formulation is used, while the convective flux is discretized using the ROE-FDS (Roe flux difference splitting) method. ROE-FDS splits the fluxes in a consistent manner and it is recommended for most cases due to its accuracy and robustness. For spatial discretization, the first-order upwind scheme was employed to perform the initial calculation only and to boost the convergence for the turbulence equations, while the flow equations (continuity, momentum and energy) were discretized using the second-order upwind scheme. Then, a higher-order, second order upwind scheme, was used to achieve a better accuracy also for the turbulence equations. The simulation procedure is shown in Figure 21. Higher order term relaxation is used, all the variables being assigned a factor of 0.25 in order to increase convergence rate especially at high Courant numbers.

The Courant Number reflects the portion of a cell that the solution will traverse by advection in one step. The Courant number is gradually increased during the simulation from 1 to 25 in order to decrease solution oscillations associated with the unstable flow and to improve the accuracy while still having a fairly decent convergence rate. Under-relaxation factors such as turbulent kinetic energy and turbulent dissipation rate are set at 0.25, while the turbulent viscosity at 0.8. The solution can become unstable and develop numerical oscillations from various reasons (skewed grids, fast increase in Courant number, ill-posed boundary conditions, highly unstable flow), therefore a relaxation factor is used (it works by taking a part of the value from the previous iteration in order to dampen the solution and reduce steep oscillations).

The reference values that were used in the case settings and results reporting can be seen in Figure 22 and Figure 23.

The convergence criteria for the normalized flow residuals was set to 10^{-5} and that the monitored coefficients (x,y and z direction force and moment) stopped oscillating

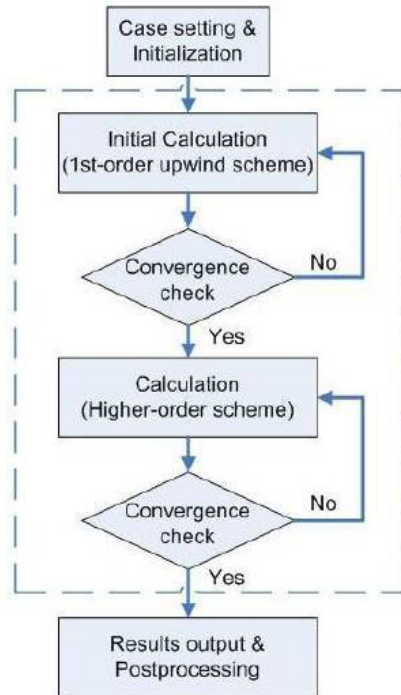


Figure 21 - Simulation flow chart

Reference Values	
Area (m ²)	91
Density (kg/m ³)	1.225064
Enthalpy (j/kg)	292594.5
Length (m)	3.5
Pressure (pascal)	101325
Temperature (k)	288.15
Velocity (m/s)	71.99563
Viscosity (kg/m-s)	1.7894e-05
Ratio of Specific Heats	1.4

Figure 22 - Reference values for FME configuration

Area (m ²)	95.92
Density (kg/m ³)	1.225064
Enthalpy (J/kg)	292594.5
Length (m)	3.5
Pressure (pascal)	101325
Temperature (K)	288.15
Velocity (m/s)	71.99563
Viscosity (kg/m-s)	1.7894e-05
Ratio of Specific Heats	1.4

Figure 23 - Reference values for WME configuration

3 CFD RESULTS

The force and moment coefficients as stated previously are referenced in the body axis system. Moreover the moments are reduced in aircrafts considered CG that is situated on the symmetry plane and on an axis parallel to the ground that passes through the aircraft's nose, see for example Figure 10.

Configuration	X_CG [m]	Y_CG [m]	Z_CG [m]
FME	14.05	0	0
WME	16.84	0	3.01

Table 1 - FME and WME CG locations

The non-dimensional coefficients for force and moment (in the x, y and z directions) are computed according to the formulas:

$$cF = \frac{Force}{0.5\rho_{ref}S_{ref}V_{ref}^2}$$

$$cM = \frac{Moment}{0.5\rho_{ref}S_{ref}l_{ref}V_{ref}^2}$$

, where the reference values are taken from Figure 22 or Figure 23 for FME and WME, respectively.

It is important to note that l_{ref} is the MAC of each configuration and S_{ref} is the wing are. In order to get the classical aerodynamic moment coefficients, roll (Cl) and yaw (Cn), one should multiply the x direction (cMx) and, respectively, the z direction (cMz) moment coefficients with the $\frac{MAC}{wing\ span}$.

3.1. Selection of Mesh Sizing

A grid sensitivity study has been carried out on the **wing mounted engines** configuration in order to obtain the grid independency of the results at the AoS = 0° case. For this purpose only the surface and volume mesh was altered without affecting the boundary layer resolution that was required by the turbulence model, the height of the first cell was kept constant to 4×10^{-4} m (corresponding to the desired y^+ value of 35) and the stretching factor of 1.2. The surface mesh and volume mesh away from the near solid surface was made **1.5** times finer for each of the grids, Coarse (11Million Cells), Medium (14 Million cells) and respectively, Fine (24 Million cells). The most relevant grid independent result is for the x-direction moment coefficient (cMx) where we expect the coefficient for AoS = 0° to become null (due to flow and geometry symmetry), the curve and the exponential fit show that the coefficient will go to 0 within a good approximation for the Fine grid. Since for the x-direction force (cFx) coefficient we have no calibration value only a sensitivity check can be plotted, and again we observe a tendency to

asymptotically reach convergence on the fine grid. In this plots we have preferred the cM_x over cM_z since the former is produced by Lift-like forces that are one order of magnitude higher than Drag-like forces (associated with cM_z), thus better showing the level of asymmetry in the solution.

The conclusion to be drawn it is that the Fine Grid should be used as reference for results reporting despite its increased size and inherent increased computational effort. For the remainder of this document only results obtained on the Fine grid are shown for both aircraft configurations. The equivalency of the Fine grid on both configurations is made through constant sizing on relevant equivalent surfaces and same sizing of the far field and the transition of the levels of grid sizing.

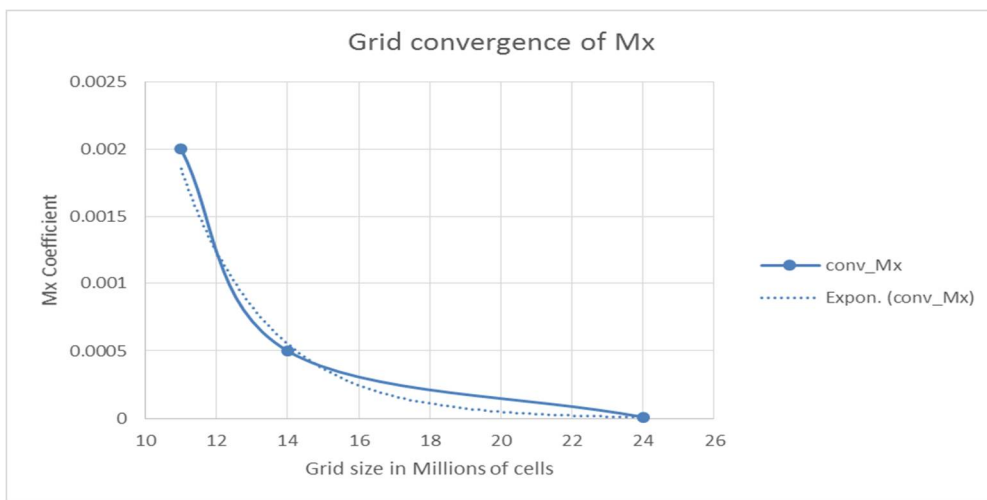


Figure 24 - Grid convergence of Mx coefficient

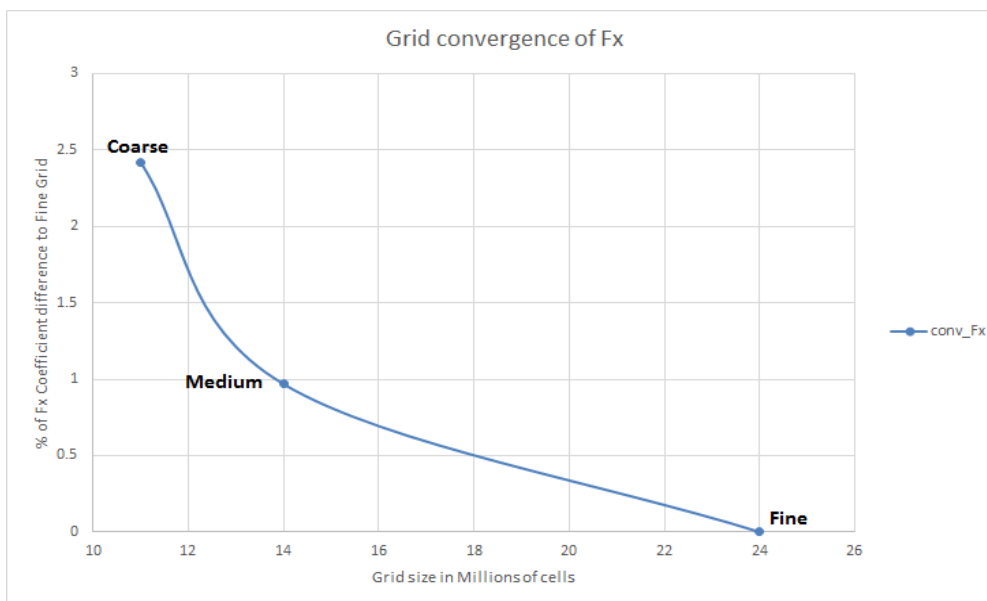


Figure 25 - Grid convergence of Fx coefficient

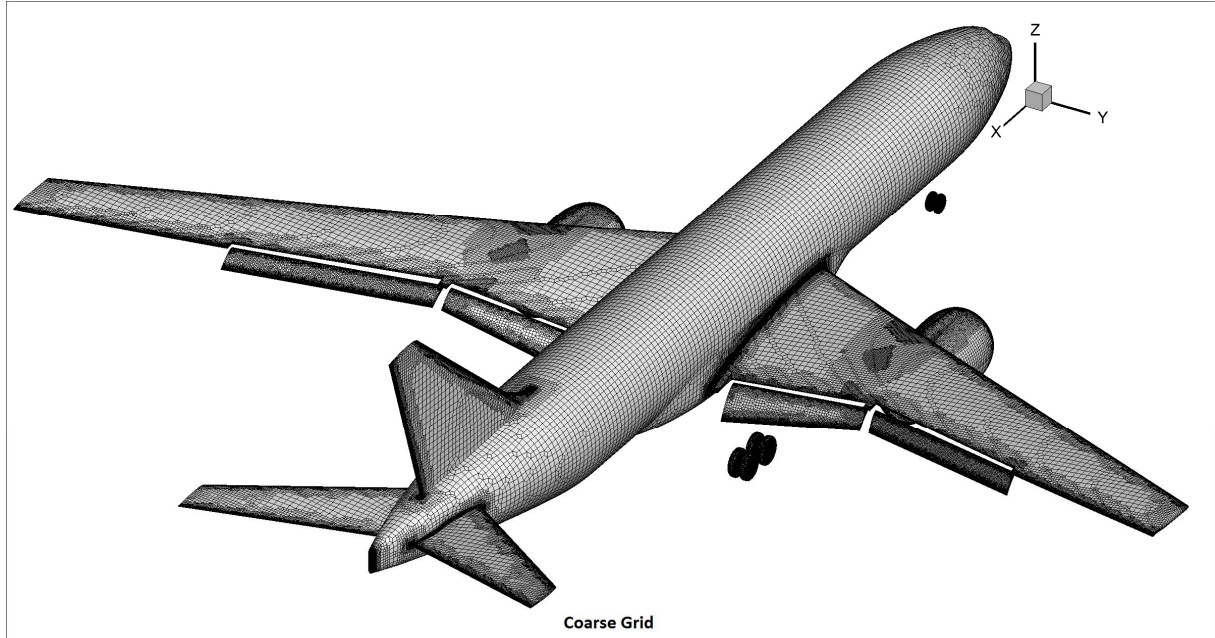


Figure 26 - Wing mounted engines configuration; Coarse Grid

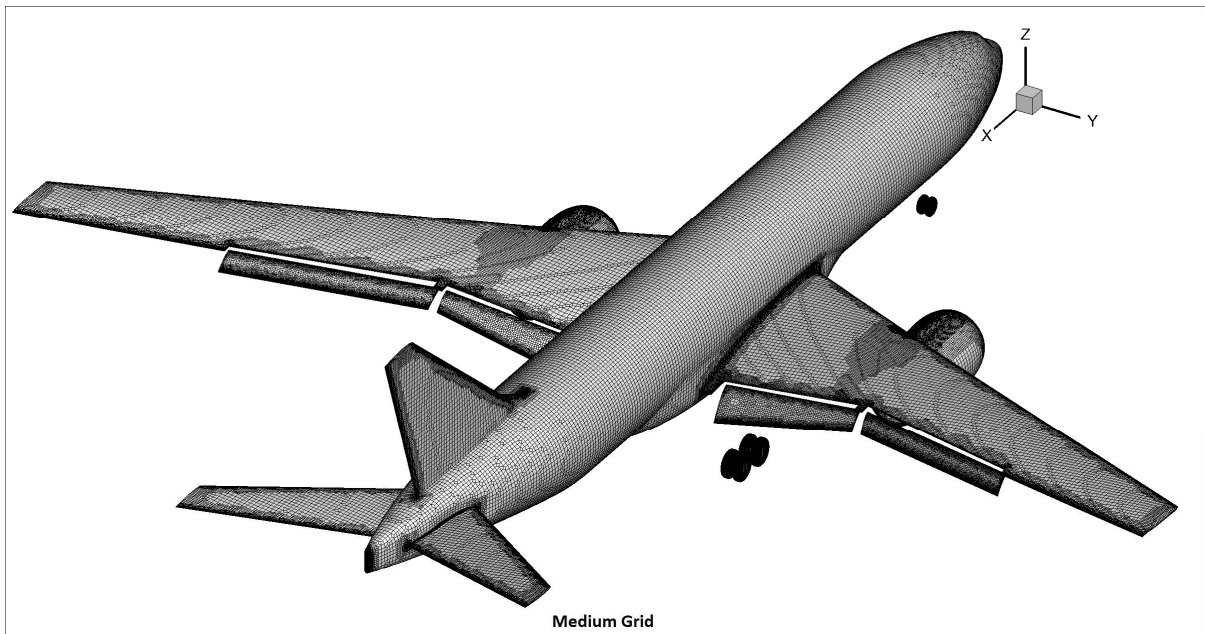


Figure 27 - Wing mounted engines configuration; Medium Grid

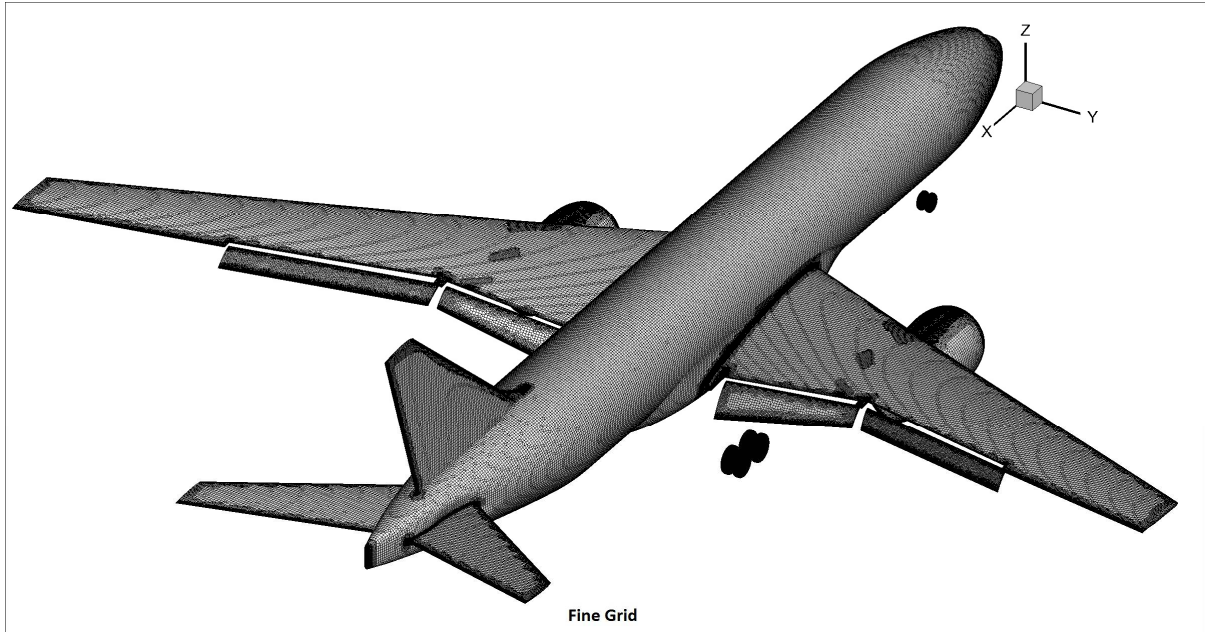


Figure 28 - Wing mounted engines configuration; Fine Grid

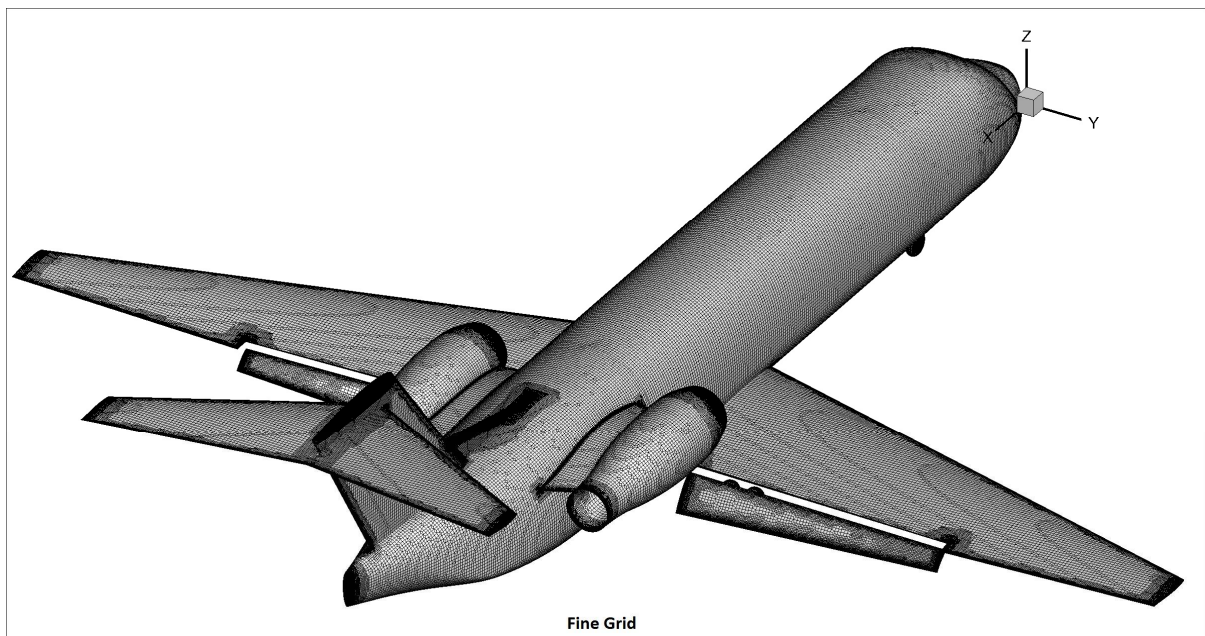


Figure 29 - Fuselage mounted engines configuration; Fine Grid

3.2. Results for Fuselage Mounted Engines Configuration

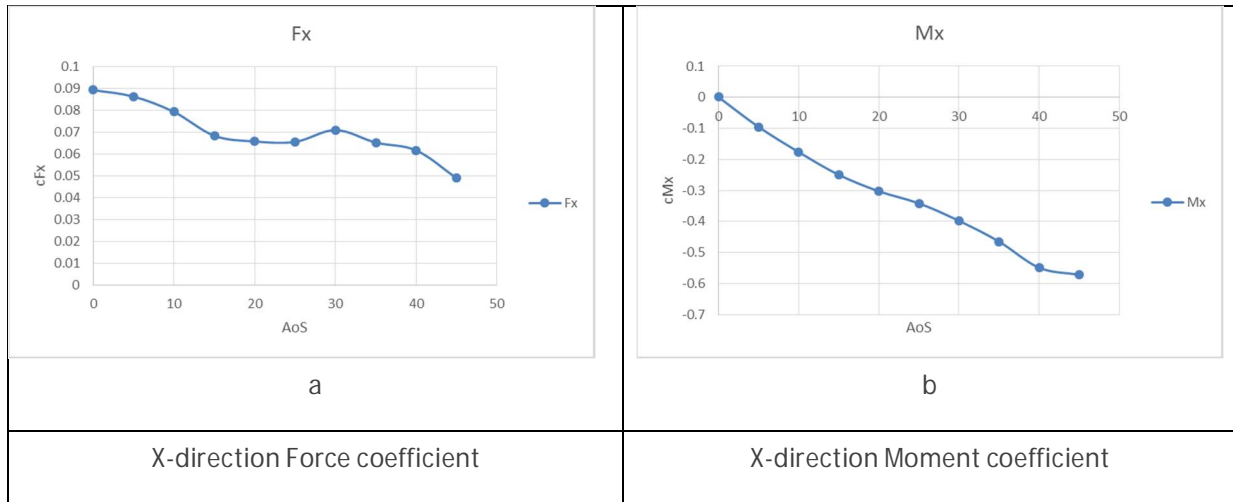


Figure 30 - X-direction force and moment coefficients

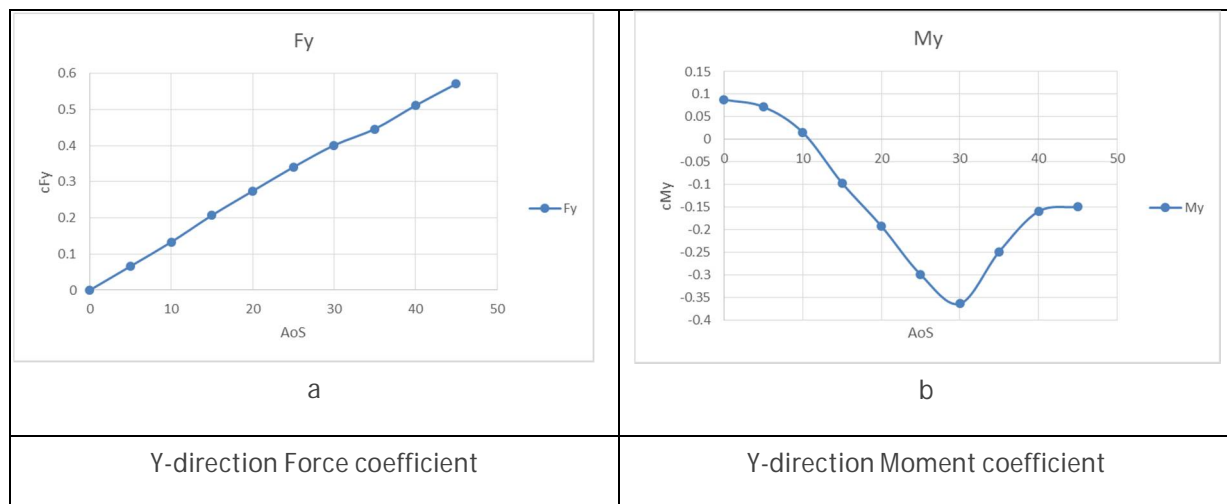


Figure 31 - Y-direction force and moment coefficients

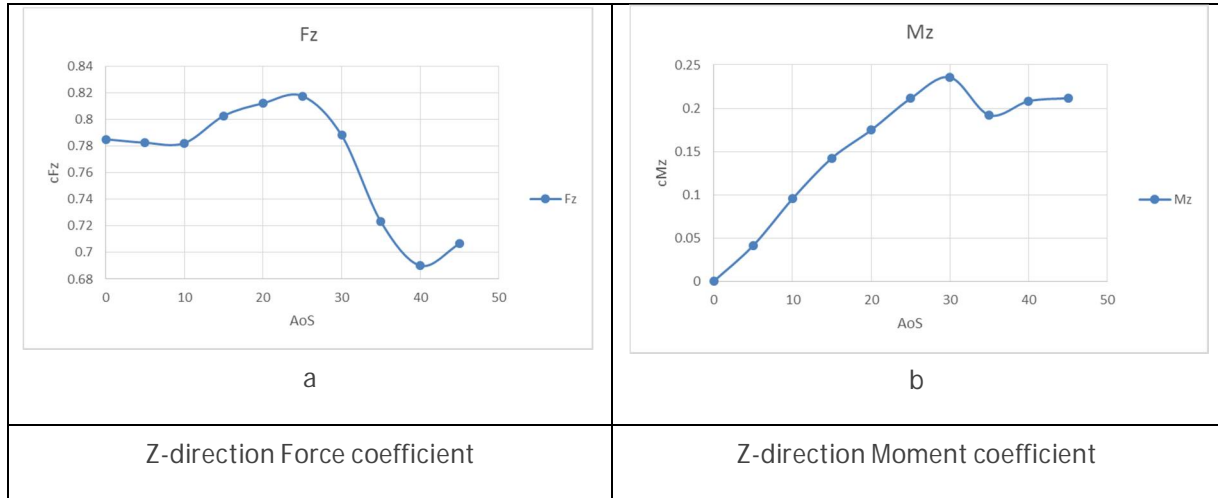


Figure 32 - Z-direction force and moment coefficients

AoS [deg.]	cFx [-]	cFy [-]	cFz [-]	cMx [-]	cMy [-]	cMz [-]
0	0.0892	0.0001	0.7853	0.0007	0.0879	0.0002
5	0.0862	0.0663	0.7827	-0.0954	0.0721	0.0413
10	0.0792	0.1332	0.7824	-0.1764	0.0155	0.0954
15	0.0683	0.2073	0.8029	-0.2496	-0.0965	0.1424
20	0.0657	0.2743	0.8124	-0.3026	-0.1921	0.1748
25	0.0655	0.3405	0.8178	-0.3417	-0.2996	0.2113
30	0.0709	0.4011	0.7882	-0.3977	-0.3641	0.2357
35	0.0652	0.4463	0.7231	-0.465	-0.2487	0.1921
40	0.0616	0.5112	0.6902	-0.549	-0.1596	0.2082
45	0.0489	0.5712	0.7067	-0.572	-0.1495	0.2116

Table 2 - FME aerodynamic coefficients

3.3. Results for Wing Mounted Engines Configuration

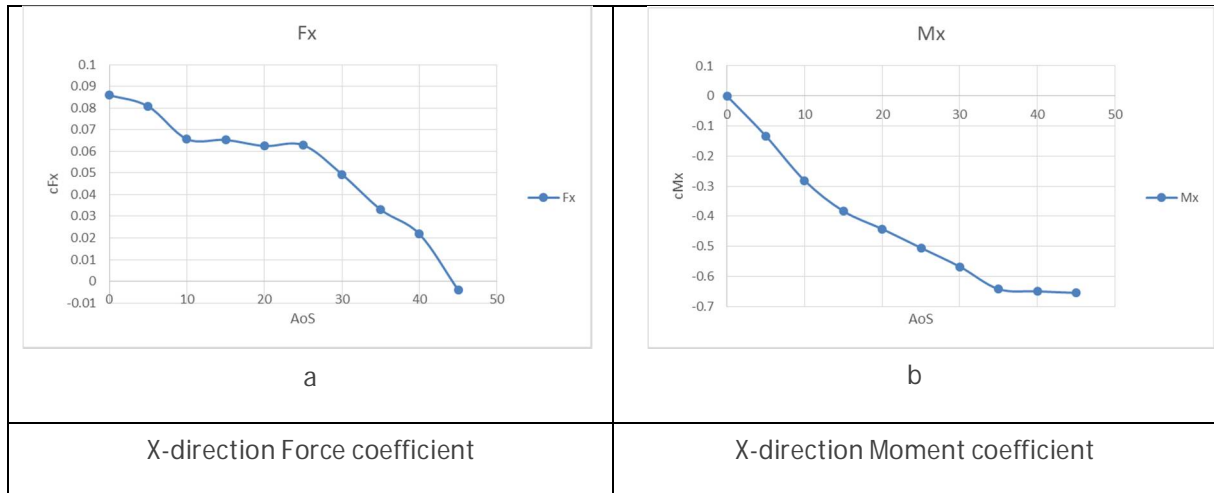


Figure 33 - X-direction force and moment coefficients

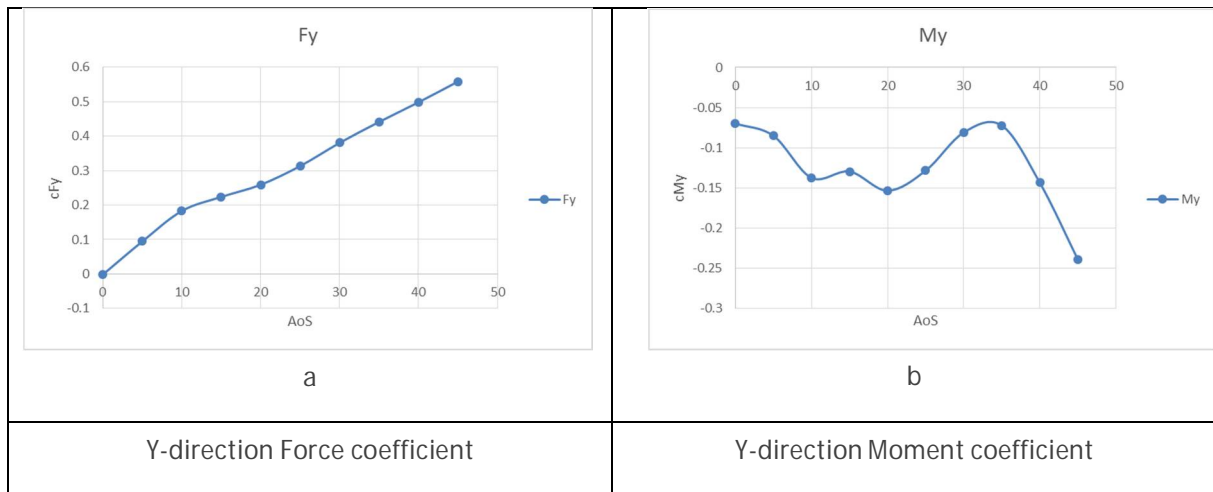


Figure 34 - Y-direction force and moment coefficients

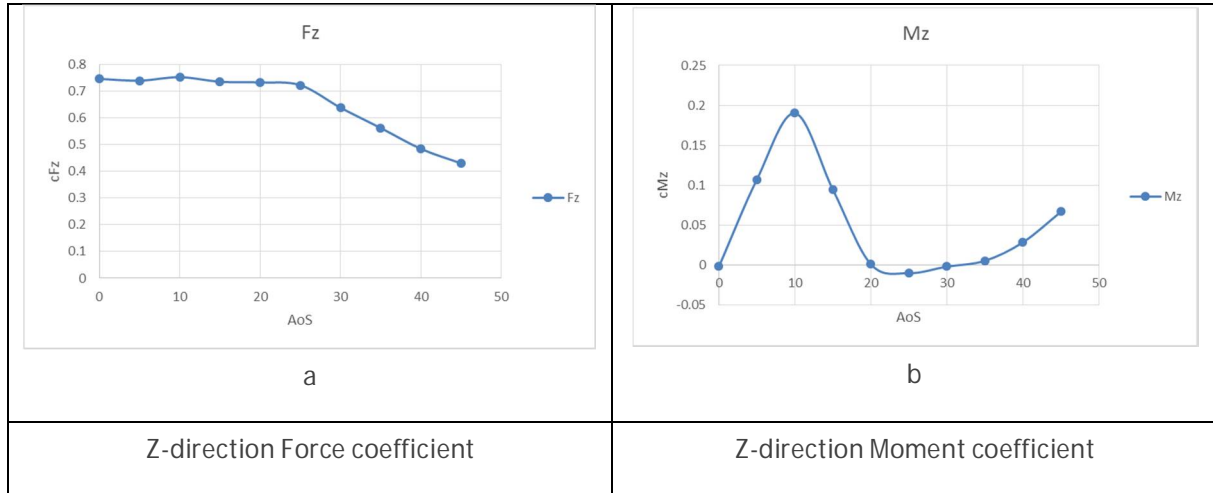


Figure 35 - Z-direction force and moment coefficients

AoS [deg.]	cFx [-]	cFy [-]	cFz [-]	cMx [-]	cMy [-]	cMz [-]
0	0.086	-0.0016	0.7473	0.00001	-0.0699	-0.0022
5	0.0808	0.0945	0.7404	-0.1332	-0.0852	0.1071
10	0.0656	0.1825	0.7532	-0.2813	-0.1372	0.1902
15	0.0653	0.2237	0.7364	-0.383	-0.1297	0.0941
20	0.0625	0.259	0.7339	-0.4424	-0.1536	0.0006
25	0.0629	0.3132	0.7235	-0.5053	-0.1286	-0.0104
30	0.0494	0.3805	0.639	-0.5678	-0.081	-0.0022
35	0.0331	0.4412	0.5631	-0.6422	-0.0724	0.0051
40	0.0218	0.4983	0.4849	-0.6498	-0.1437	0.0283
45	-0.0041	0.5584	0.4306	-0.655	-0.2395	0.0666

Table 3 - WME aerodynamic coefficients

3.4. Similarities and Discrepancies in between the Models

In the dynamic and lateral control analysis for an aircraft in crosswind and slippery runway the yawing moment (Mz) and lateral force (Fy) have the most relevant importance.

- For **FME configuration** this values are given in Figure 32 b, respectively, in Figure 31 a. It can be seen that the lateral force is almost linear with a small kink at the vertical tail stall AoS (30deg.) and a notable loss in cMz in a range of AoS from 30 to 45 deg. This can be also explained in the detailed breakdown of the yawing moment coefficient (cMz) that is given in **Error! Reference source not found.**

A/C component	cMz_20deg	cMz_30deg	cMz_35deg
fuselage	-0.2655	-0.3526	-0.3891
ht	0.0256	0.0164	0.0156
lg_front	-0.0060	-0.0088	-0.0106
lg_main	0.0019	0.0025	0.0029
nacelle_l	0.0043	0.0052	0.0058
nacelle_r	0.0338	0.0397	0.0450
vt	0.3651	0.5174	0.5003
wing_l	0.0599	0.0562	0.0535
wing_r	-0.0443	-0.0401	-0.0312
Destabilizing yaw moment contributiont	-0.3158	-0.4016	-0.4310
Stabilizing yaw moment contributiont	0.4906	0.6372	0.6231
Total Mz moment coefficient	0.1748	0.2357	0.1922

Table 4 - FME cMz breakdown at AoS 20, 30 and 35 deg

- For **WME configuration** this values are given in Figure 35 b, respectively, in Figure 34 a. It can be seen that the lateral force is linear up to 10 deg. with a small kink at the vertical tail stall AoS (10deg.) and a catastrophic loss in cMz in a range of AoS from 10 to 35 deg. This can be also explained in the detailed breakdown of the yawing moment coefficient (cMz) that is given in Table 5. This loss of cMz is due to the small vertical tail volume and stall of the vertical tail and the fact that the cMz on the fuselage and nacelles increases faster than it decreases on the vertical tail.

A/C component	cMz_5deg	cMz 15deg	cMz_25deg
fuselage	-0.047065	-0.14830	-0.248841
ht	-0.00351	-0.01276	-0.0306496
lg_front	-0.00027	-0.00332	-0.0049779
lg_main	0.000732	0.00172	0.00252646
nacelle_l	-0.002622	-0.01999	-0.0299148
nacelle_r	-0.012785	-0.02579	-0.0406843
pylon_l	-0.000408	-0.00230	-0.0036029
pylon_r	-0.000849	-0.00181	-0.0024656
vt	0.1796339	0.31462	0.35467964
wing_l	0.0746751	0.06402	0.05350149
wing_r	-0.080481	-0.07184	-0.06002
Destabilizing yaw moment contributiont	-0.14799	-0.28611	-0.421156
Stabilizing yaw moment contributiont	0.255041	0.380362695	0.41070758
Total Mz moment coefficient	0.1070509	0.09425	-0.0104484

Table 5 - WME cMz breakdown at AoS 5, 15 and 25 deg.

- The increase of cFz seen at the stall of the vertical tail, 30 deg. for FME and 10 deg. for WME is explained by the fact that the horizontal tail is in the wake of the vertical tail, with an import change in the surface pressure distribution.
- The decrease in down-force on the horizontal tail mentioned previously has an effect on cMy by increasing it, at AoS > 30 deg. (FME) and at AoS 15 deg. (WME). This effect is more pronounced on the FME configuration since the wake of the stalled vertical tail affects the horizontal tail's suction surface, whereas for the WME it affects the horizontal tail's pressure surface. See Figure 31 b and Figure 34 b. The increase in cMy affects the reaction force on the front landing gear.
- The T-tail of the FME performs better at high AoS due to the end-plate effect created by the horizontal tail.
- In both FME and WME at stall and post stall of the vertical tail the cFx increases locally.

4 CONCLUSIONS AND RECOMMENDATIONS

4.1. Conclusions

The importance of a study of the aircraft aerodynamics in crosswind at high sideslip and ground effect is related to a confident dynamic simulation of the airplane mechanics in rolling travel at Take off and Landing. The main conclusions from the study are:

1. This report is a complex research activity which aims with practical results about the aerodynamic coefficients for two aircraft models in crosswind and ground effects.
2. The aerodynamic mesh used in Computational Fluid Dynamics (CFD) simulation, were calibrated with specific methods as the results to be "stable" and converge to a realistic solution.
3. The aerodynamic forces and moment coefficients were given in an aircraft body system that is clearly presented. The specific notation of the coefficients is also presented in the study.
4. The lateral stability of the Fuselage Mounted Engine (FME) is considered to be normal for the whole span of Angle of Side-Slip (AoS) studied, proved by the value and the behavior of the lateral aerodynamic coefficients.
5. The lateral stability of the Wing Mounted Engine (WME) is considered to be normal for a limited range of Angle of Side-Slip (AoS) of up to 10 degrees. This is due to the small vertical tail volume and engine arrangement in front of the Centre of Gravity (CG).
6. The influence and interference of different aircraft components is analyzed for the most relevant aerodynamic coefficients.
7. Yawing moment breakdown at high sideslip angles gives confident information about specific flow separation.

4.2. Recommendations

- It is important to obtain sufficient confidence in the aerodynamic input data to be used: the more accurate the aerodynamic input is, the more reliable the dynamic simulation results will become.
- The current configurations are limited in their nature by being only studied numerically, therefore similar wind tunnel tests are useful for validation of aircraft in high-lift configurations, in high crosswind conditions and in ground effect.

5 REFERENCES

1. ANSYS, Inc., Ansys Fluent Theory Guide, Release 15.0, Canonsburg, PA, ANSYS, Inc., 2013
2. FAA Safety Course: ALC-34: Manoeuvring: Approach and Landing
3. Ferziger J.H. and Peric M., Computational Methods for Fluid Dynamics, Third Edition, Berlin, Germany, Springer, 2002, ISBN: 3-540-42074-6
4. Hirsch C., Numerical Computation of Internal and External Flows: The Fundamentals of Computational Fluid Dynamics, Second Edition, Oxford, England, Butterworth-Heinemann, 2007, ISBN: 978-0-75-066594-0
5. Paul Jackson, Jane's all the world's aircraft 1996-97, Jane's Information Group, 1996, ISBN: 978-0710613776
6. Raymer Daniel P., Aircraft Design: A conceptual approach, Fourth edition, Playa del Rey, California, Conceptual Research Corporation, 2006, ISBN: 1-56347-829-3
7. Sadraey M., Aircraft Design: A systems engineering approach, Wiley, 2012, ISBN: 978-1119953401
8. Torenbeek E., Synthesis of Subsonic Airplane Design, Dordrecht, The Netherlands, Kluwer Academic Publishers, 1982, ISBN: 90-247-2724-3
9. Versteeg H.K. and Malalasekera W., Introduction to Computational Fluid Dynamics, The Finite Volume Method, Second Edition, Essex, England, Pearson Education Limited, 2007, ISBN: 978-0-13-127498-3
10. commonresearchmodel.larc.nasa.gov/geometry/step-files/
11. commonresearchmodel.larc.nasa.gov/geometry/vertical-tail-geometry/
12. Boeing STATSUM, Statistical Summary of Commercial Jet Airplane Accidents, Worldwide Operations 1959-2012, SKYbrary 2013
13. Martin E. Bayers, L. Ericson, Flow Physics of Transport Aircraft in Crosswind Landing Maneuvers, AIAA-2001-0693
14. Chin-Tang Weng, C. Edward Lan, Ching-Shun Ho, Dynamic Ground Effect for a Jet Transport in Crosswind, AIAA 2004-5066

Appendix A Pressure coefficient contours

Appendix A.1 Cp Contours for FME

Cp contours are given for the FME configuration on the upper and lower side.

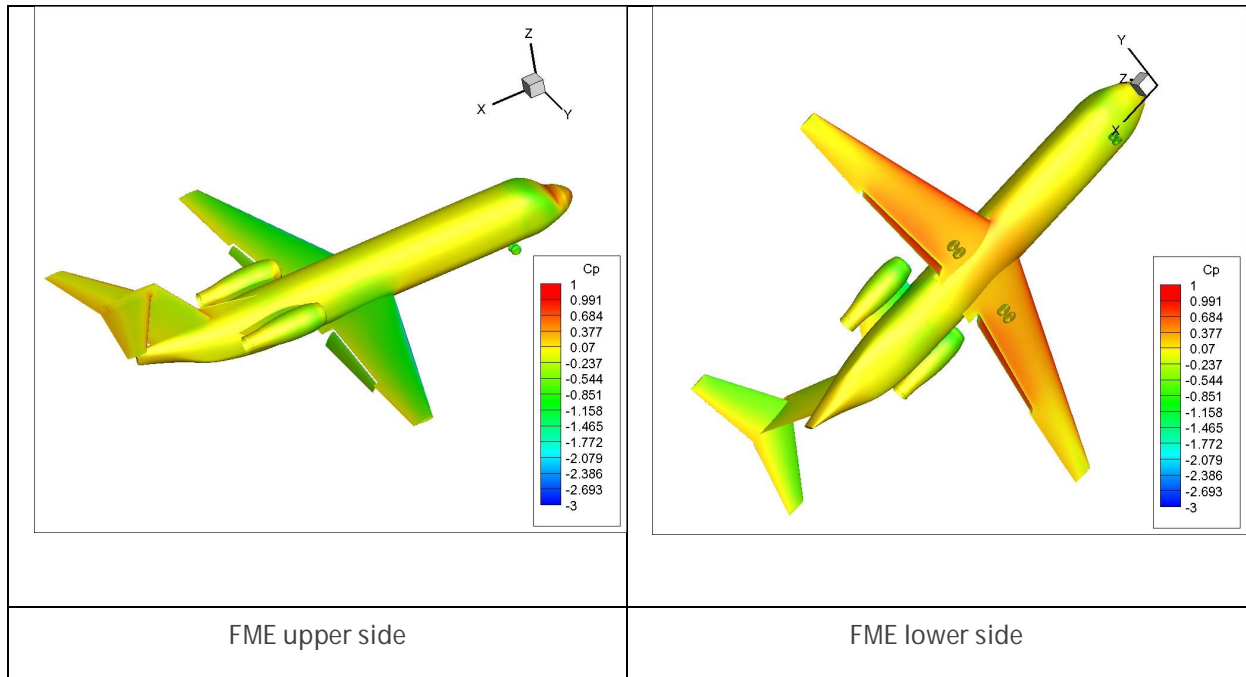


Figure 36 - Cp at AoS = 0 deg.

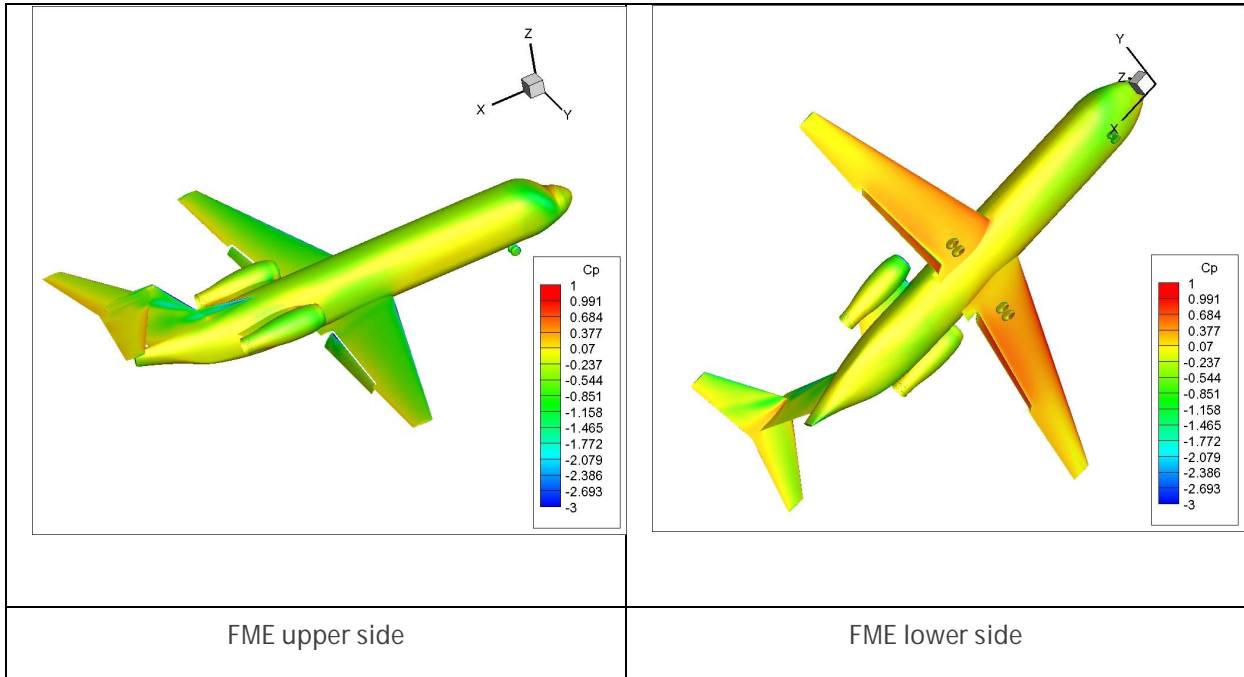


Figure 37 - Cp at AoS = 20 deg.

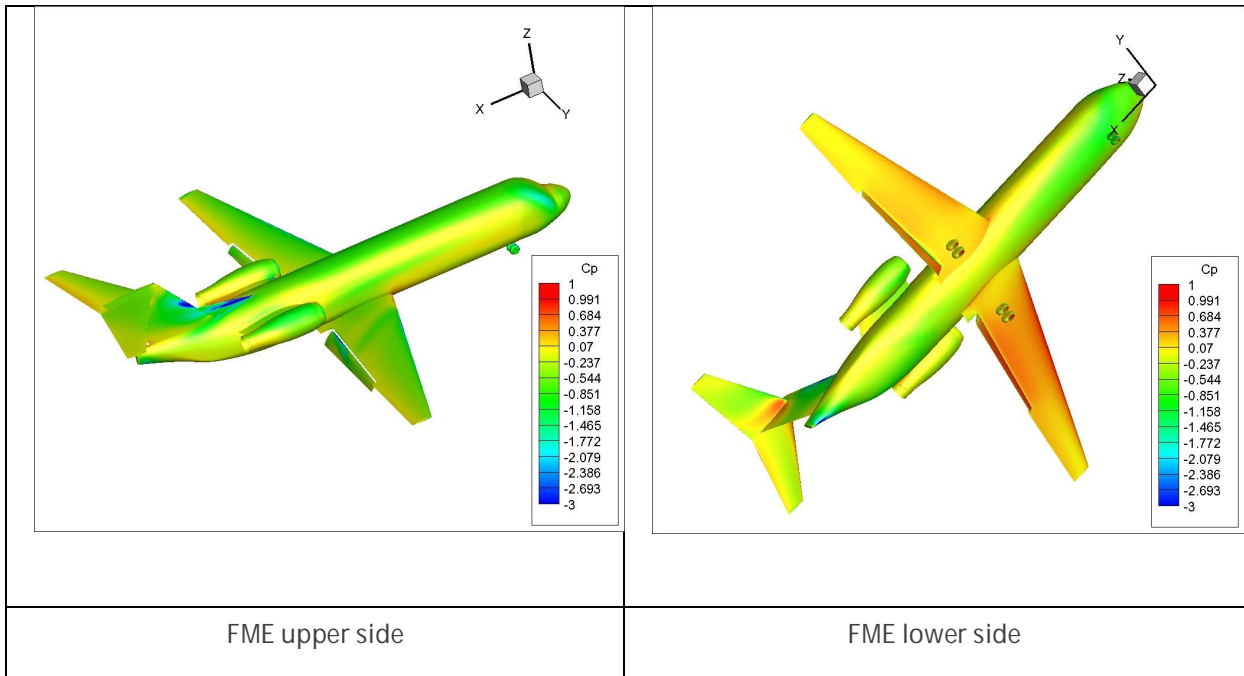


Figure 38 - Cp at AoS = 30 deg.

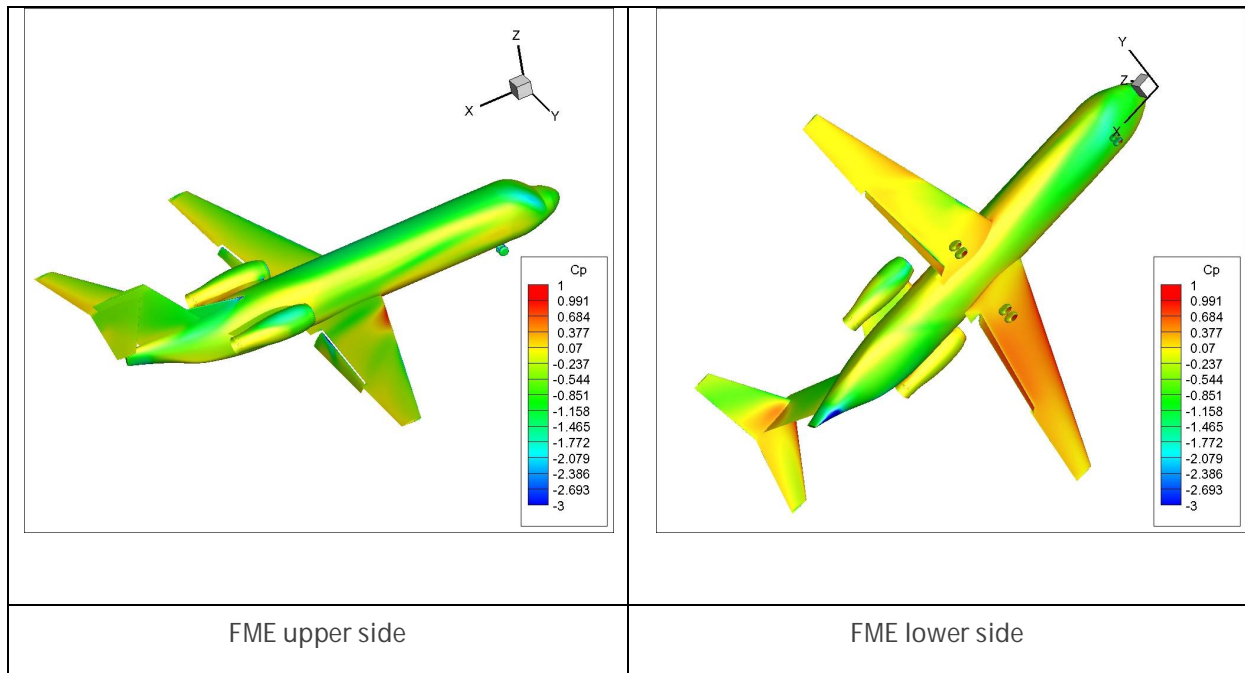


Figure 39 - Cp at AoS = 40 deg.

Appendix A.2 Cp Contours for WME

Cp contours are given for the WME configuration on the upper and lower side.

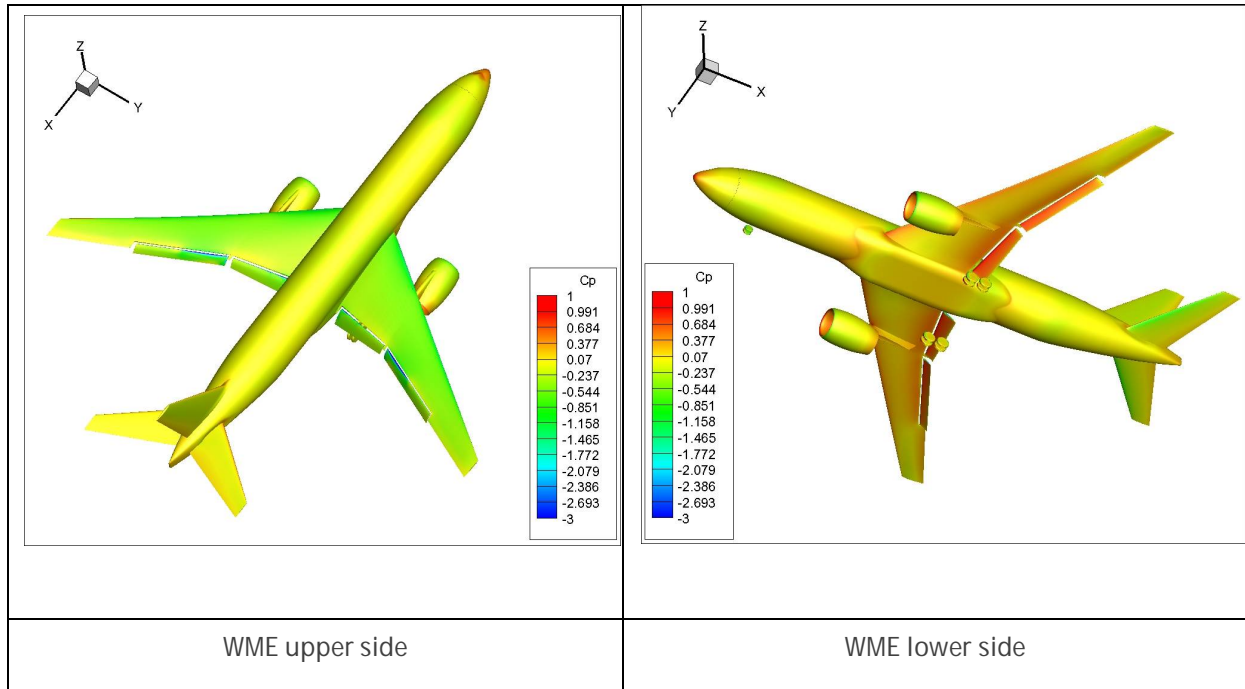


Figure 40 - Cp at AoS = 0 deg.

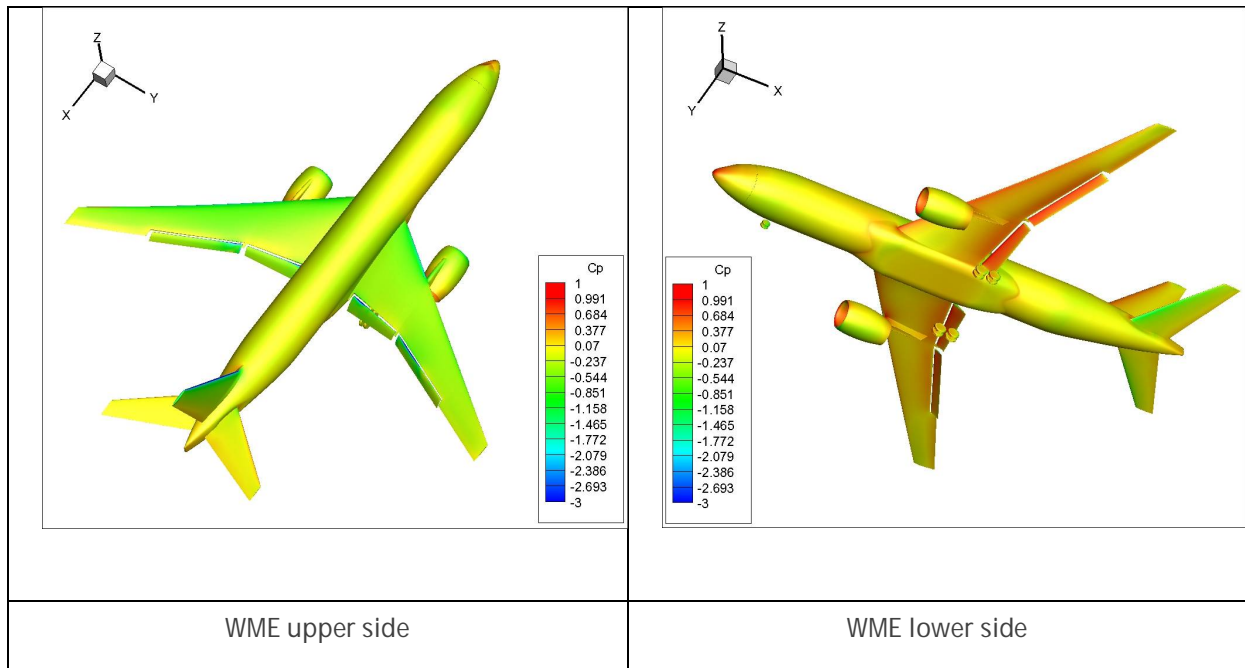


Figure 41 - Cp at AoS = 10 deg.

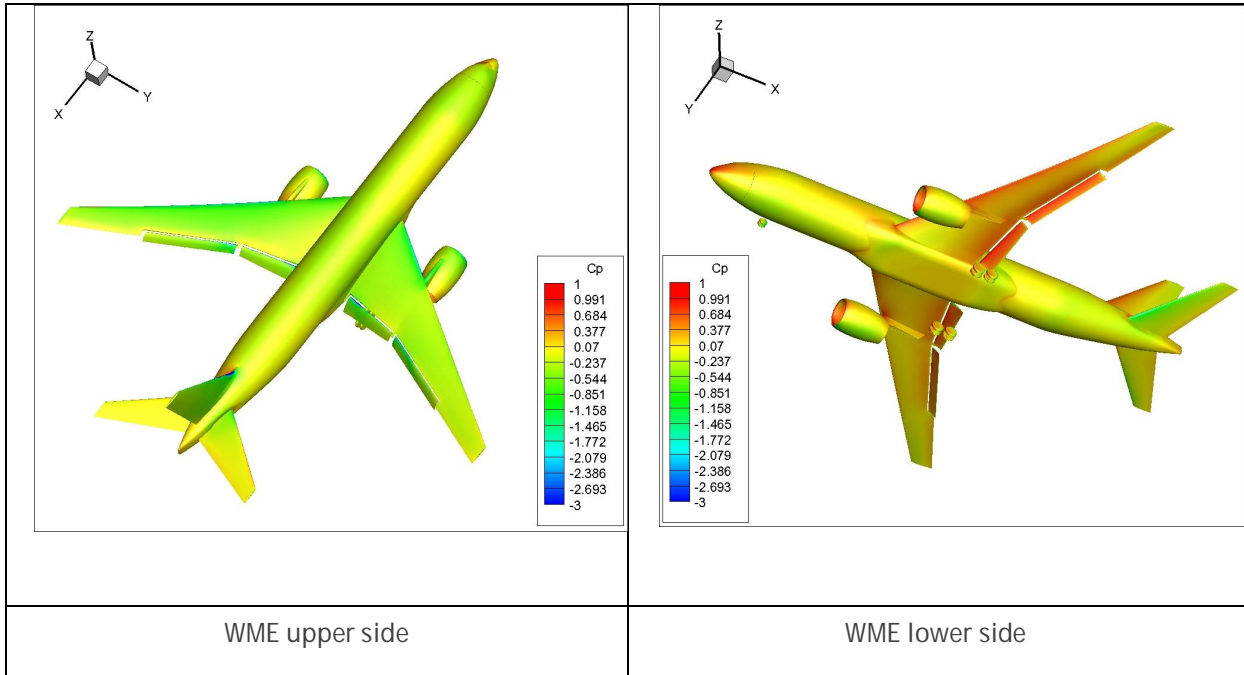


Figure 42 - Cp at AoS = 15 deg.

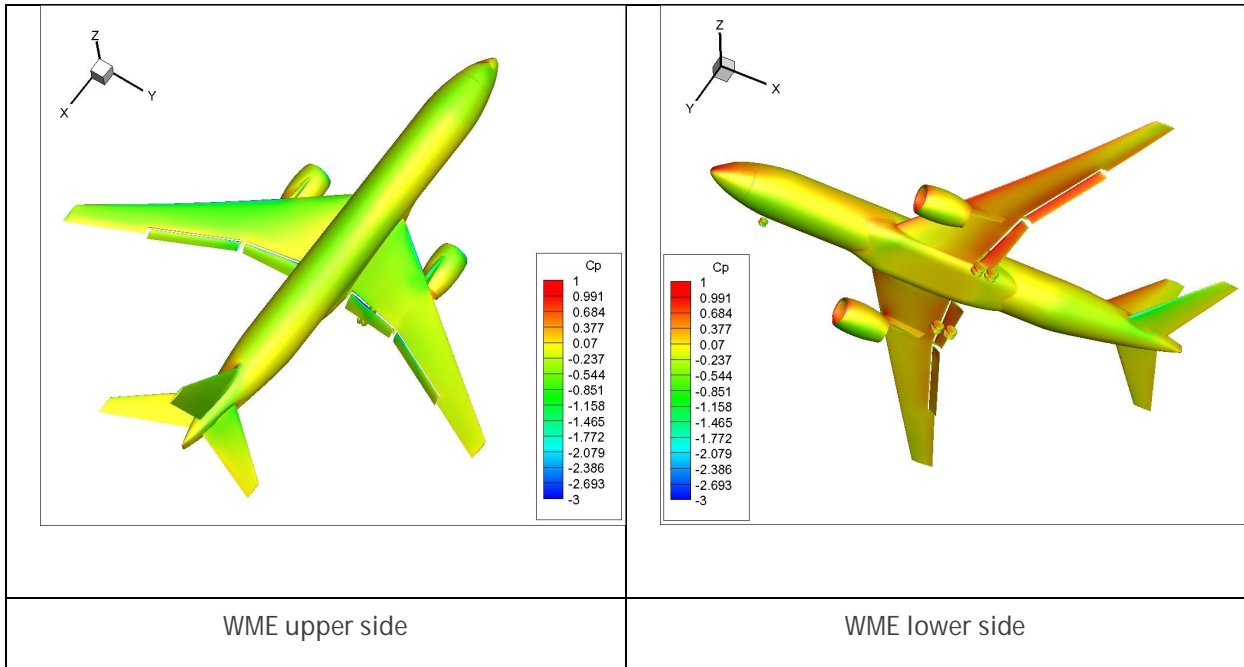


Figure 43 - Cp at AoS = 20 deg.